Doctoral Thesis

Visual Information Processing and Integration Mechanism of Cat Early Visual Pathway

ネコ初期視覚経路における視覚情報処理及び統合メカニズム

Naofumi Suematsu

Laboratory of Cognitive and Behavioral Neuroscience,

Graduate School of Frontier Biosciences,

Osaka University

Supervisor

Prof. Hiromichi Sato

March 2014

Table of Contents

Summary....5

General Introduction....6

Background....6

The Aim of Theme 1....7

The Aim of Theme 2....7

Complements to General Introduction....9

Early Visual Pathway....9

Receptive Field....9

Reverse Correlation....10

Cross Correlation....10

Singular Value Decomposition....11

Figures....12

References....16

Theme 1....19

Abstract....20

Introduction....21

Methods....23

Preparation....23

Visual Stimulation and Recording Protocols....24

Receptive Field Fitting....27

Orientation Tuning....28

Response Prediction from the Linear Receptive Field....29
Static Non-linear Response Modulation Function....30
Histology....31
Results....32
SF×ORI Map and Orientation Tunings of LGN Neurons....32
Predicted Orientation Tunings from a Linear Receptive Field....34
Grid Size Effect on Predictions....37
Static Non-linear Response Modulation Function....39
Discussions....42
Two Possible Mechanisms for an Elongated Classical Receptive Field....43
Origin of the Non-linear Response Modulation....44
The Functional Significance of Orientation-tuned Non-linear Response Modulation....45
Figures....47
References....55

Theme 2....60
Abstract....61
Introduction....62
Methods....64
Preparation....64
Visual Stimulation, Recordings, and On-line Data Analysis....65
Off-line Data Analysis....66
Histology of the LGN....69
Results....71

Comparison of Spatial RF Structures of RGCs and LGN neurons.....71
Relationship of Spatial RF Structures of Connected pairs.....73
Comparison between Same- and Opposite-Response-Sign Pairs.....74
Comparison of Temporal RF Structures of Connected Pairs.....79
Discussions.....81
Spatial RF Structure of RGCs.....81
Retinogeniculate Connections and Response-Signs.....82
Efficacy and Contribution, and RF Property.....85
Temporal RF Structures of Retinogeniculate-Connected Pairs.....86
Figures.....88
References.....99

Conclusions.....108
Acknowledgements.....109
Research Achievements.....110

Summary

Receptive field (RF) properties are key features of neurons in the early visual pathway, and understanding these basic features is essential to understand further neural functions in our brain. Here I show that the orientation tuning property of cat lateral geniculate nucleus (LGN) neurons are generated by their elliptical RF structure and orientation-selective nonlinear inputs, and that the RF structure of a single LGN neuron is inherited from the convergent inputs from multiple retinal ganglion cells. These results suggest that the stimulus-specificity of the cat early visual system starts from the retina and that the elaboration of tuning properties progresses at each stage in the pathway.

General Introduction

Background

In the early visual system of mammals, visual information is received by the retina and then relayed to the primary visual cortex (V1) via the lateral geniculate nucleus (LGN) (Figure 0.1A). Through these stages, receptive field (RF, the area on which neurons respond to visual stimuli presented, see Complements to General Introduction) properties, such as orientation (e.g. tilt of a bar)-, spatial frequency (e.g. thickness of a bar)-, and temporal frequency (e.g. speed of a bar)-tunings (Figure 0.2), are successively elaborated, which enhances the sensitivity for various visual features in neurons of the early visual system (Hubel and Wiesel, 1959, 1962; Enroth-Cugell and Robson, 1966; Campbell et al., 1969; Movshon et al., 1978; Derrington and Fuchs, 1979; Frishman et al., 1987).

In the LGN of cats and monkeys, it had been commonly believed that neurons exhibit only weak or no orientation selectivity, and their RFs are almost circular (Hubel and Wiesel, 1959, 1962, 1977). However, more recent studies have reported that LGN neurons exhibit moderate orientation sensitivity in cat (Soodak et al., 1987; Shou and Leventhal, 1989; Smith et al., 1990), mouse (Scholl et al., 2013; Zhao et al., 2013; Niell, 2013), and marmoset (Cheong et al., 2013) due to an elliptical RF structure (Soodak et al., 1987; Ahmed and Hammond, 1991). Meanwhile, it has been suggested that the non-linear response modulation from outside the classical RF (CRF) was sensitive to the stimulus orientation (Sillito et al., 1993; Sun et al., 2004; Naito et al., 2007), suggesting an elliptical CRF alone does not explain the orientation selectivity. In other words, there is a possibility that even when the CRF is completely circular, LGN neurons exhibit a significant orientation tuning due to a simultaneous stimulation of CRF and outside the CRF which induces orientation-sensitive surround suppression.

This doctoral thesis consists with studies on two themes: theme 1, spatiotemporal RF structure

of LGN neurons, and 2, connection rules of retinogeniculate projection underlying the RF structure of LGN neurons.

The Aim of Theme 1

In this study, I directly described the spatiotemporal RF structure of cat LGN neurons using a reverse correlation method (red and blue arrows in Figure 0.3, the image averaging of the stimuli extracted based on the neural activity timing, see Complements to General Introduction) with dynamic noise stimuli. I found that a certain population of LGN neurons exhibit significantly elongated RF structures and that the long axes of the RF structure of individual neurons corresponds to their preferred orientations. Additionally, the measured orientation tuning was significantly sharper than that predicted from the RF structure. My results suggest that orientation-tuned non-linear operations between linear products from the RF and spiking response contribute to orientation tuning in the LGN and that this is due to suppressive modulation elicited by a stimulation of outside the RF (Suematsu et al., 2012).

The Aim of Theme 2

However, there were still questions: how the elliptical RF structure of LGN neurons is generated, and how the orientation tuning of LGN neurons contributes to that of V1 neurons. Then, in this study, I investigated the mechanisms generating the RF structure of cat LGN neurons, conducting simultaneous recordings of retinal ganglion cells (RGCs) and LGN neurons monosynaptically connected with the RGCs, which were confirmed with cross-correlation analysis method (green arrows in Figure 0.3, resultant correlogram is the time histogram of the LGN neural activity aligned with the RGC activity, see Complements to General Introduction), and found that RGCs and LGN neurons exhibited similarly elliptical spatial RF structures, and that an RGC projection of the same response sign was the

primary contributor to the generation of the CRF center of the LGN neuron, while an RGC projection of the opposite response sign was responsible for enhancing the antagonistic surround of CRF. In addition, singular value decomposition, which extracts a spatiotemporal RF structure into a spatial structure, temporal structure, and their contributions to the original structure (brown arrow in Figure 0.3, see Complements to General Introduction), revealed that the temporal RF structure of an RGC was tightly correlated with its target LGN neuron. These results suggest that the elongated RF of LGN neurons is mainly inherited from that of the primary-projecting RGC and that convergent inputs from multiple RGCs improve the stimulus feature sensitivity of LGN neurons, presumably contributing to efficient processing in the visual cortex (Suematsu et al., 2013).

Complements to General Introduction

Early Visual Pathway

Generally, in mammal, photoreceptor cells in retina receive light and convert the intensity into the graded electrical potentials, then horizontal, bipolar, and amacrine cells convey and process the signal, and RGCs convert the amplitude into the firing frequency of action potentials and output to LGN as well as to the superior colliculus. LGN contains two kinds of neurons: relay cells and interneurons. Relay cells are excitatory neurons, which project to V1 and the perigeniculate nucleus (PGN). They also receive excitatory feedback input from V1 as well as feedforward input from retina and inhibitory inputs from local interneurons and PGN neurons. That is, relay cells receive recurrent inhibitory feedback signal via PGN neurons. Moreover, since V1 neurons send excitatory signals to PGN neurons and interneurons in LGN, relay cells receive inhibitory feedback signal from V1 indirectly (Figure 0.1B).

It is commonly thought that retinogeniculate connections are one-to-one or one-to-many (divergent); there are no many-to-one (convergent) connections. However, my data suggest the existence of convergent retinogeniculate connections, and I obtained a small but certain examples of the convergent connections (Figures 2.2B and C). These data suggest that relay cells do not simply relay the signals; instead, they are involved in a generation of the stimulus-specificity.

Receptive Field

Receptive field (RF) is the conceptual area sensitive to the stimulus inputs. When a kind of stimuli is inputed in RF, the neuron can respond to the stimulus. This term has been used originally in the field of the investigation of somatosensory system, and, then, visual and auditory systems. In visual system, RF refers to the spatial and temporal extent on which neurons respond to visual stimuli presented (Figure 0.4). One of the most important preferences of RF is response sign: ON and OFF. ON

region is sensitive to the visual stimulus "on" (becoming brighter), and OFF region to the "off" (becoming darker). Generally, RGCs and LGN neurons exhibit ON (OFF)-center and OFF (ON)-surround RF structure, which are expressed by Difference of Gaussians (DoG) model:

$$DoG(x) = C \exp[-(x/\sigma_c)^2] - S \exp[-(x/\sigma_s)^2] \quad (0.1)$$

, where x is a spatial position, C and σ_c indicate intensity and spatial extent of center Gaussian, respectively, and S and σ_s are those of surround Gaussian. In this doctoral thesis, however, I used modified version of DoG model (Equations 1.1–1.7) because I wanted to parameterize RF orientation too.

Reverse Correlation

Reverse correlation is the method in order to quantitatively and precisely measure the RF spatial extent and other kind of preferences. In this doctoral thesis, I used spike triggered average (STA) of reverse correlation, which allows me to obtain the linear RF structure ("linear" in here means "directly inherited from inputs"). STA is the simplest submethod, averaging the visual stimuli themselves (or their properties) extracted based on spike timings. When I average the stimuli presented at a particular time, which corresponds to response latency, before a spike, I will obtain the RF structure exhibiting maximum response. Changing the trace-back time, I will finally obtain the spatiotemporal RF structure.

Cross Correlation

Cross correlation is essential to confirm the functional connections between two neurons. The calculation is similar to STA, aligning the spikes of one neuron with the other neuron. The existence of a functional connection is defined by the number of spikes of the aligned neuron; the neuron is excited by

the other neuron if the number of spikes is significantly higher than a particular criterion, and vice versa. In theme 2, in order to confirm the excitatory projection from an RGC to an LGN neuron, the spikes of an LGN neuron were aligned with those of an RGC, and the pair was defined as sharing a functional connection when the resultant number of spikes was higher than a criterion (baseline mean + 5SD).

Singular Value Decomposition

To obtain a temporal RF structure, I conducted singular value decomposition (SVD) of a spatiotemporal RF structure. SVD splits an m × n matrix into three components: an m × m unitary matrix, an m × n diagonal matrix, and n × n unitary matrix. In practice, I preprocessed a three-dimensional (space × space × time) RF structure deforming into two-dimensional (space × time) matrix, then applied SVD to the 2D matrix, and finally obtained spatial and temporal RF structures, and their contributions to the original matrix. Although there are several ways to obtain temporal RF structures (e.g. spatial summation of RF structure of each latency), I used SVD because of its robustness to some noisy values in spatiotemporal RF structure, which were resulted from finite recording time.

Figures

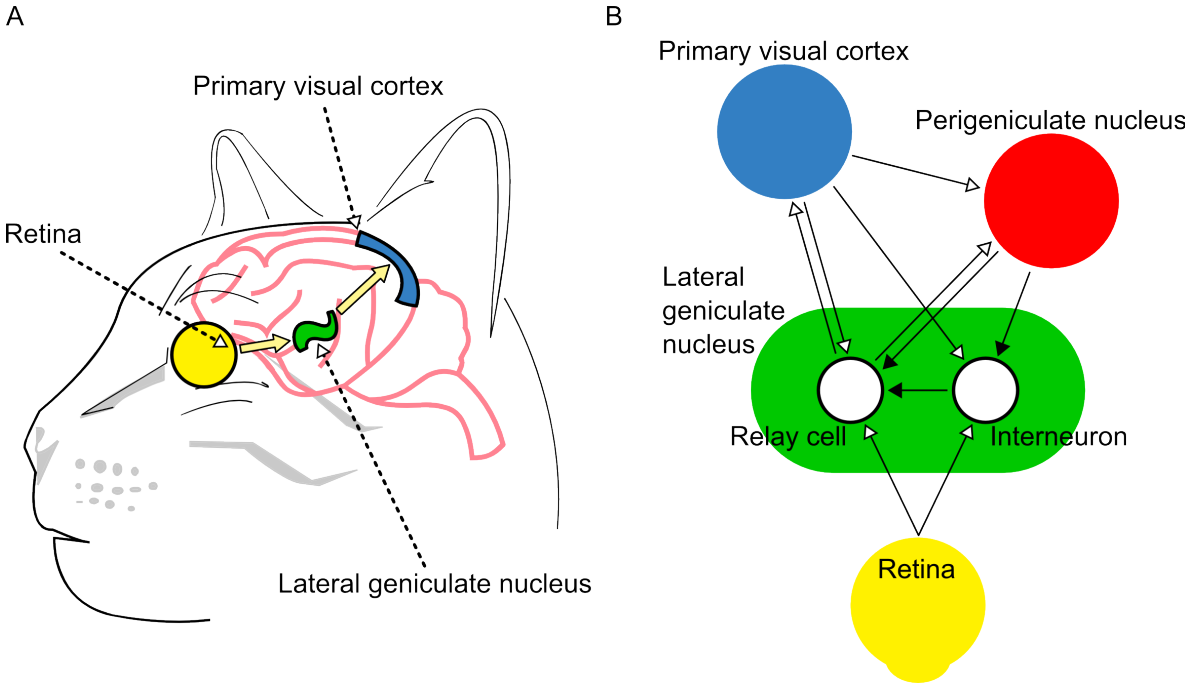

Figure 0.1: A) Early visual system of cat. B) more detailed schema. Open and filled arrows indicate excitatory and inhibitory projections, respectively.

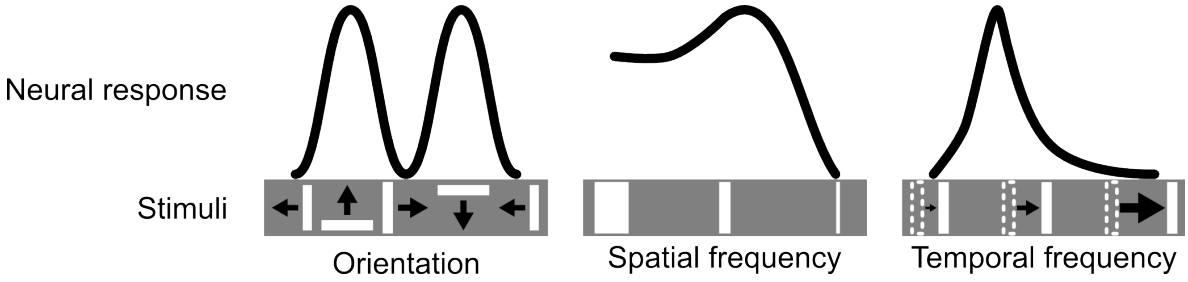

Figure 0.2: Examples of RF property tuning (left to right, orientation-, SF-, and TF-tunings). This example neuron has orientation selectivity to a vertically-moving bar, SF selectivity to a middle (and also wide)-width bar, and TF selectivity to a middle-speed bar.

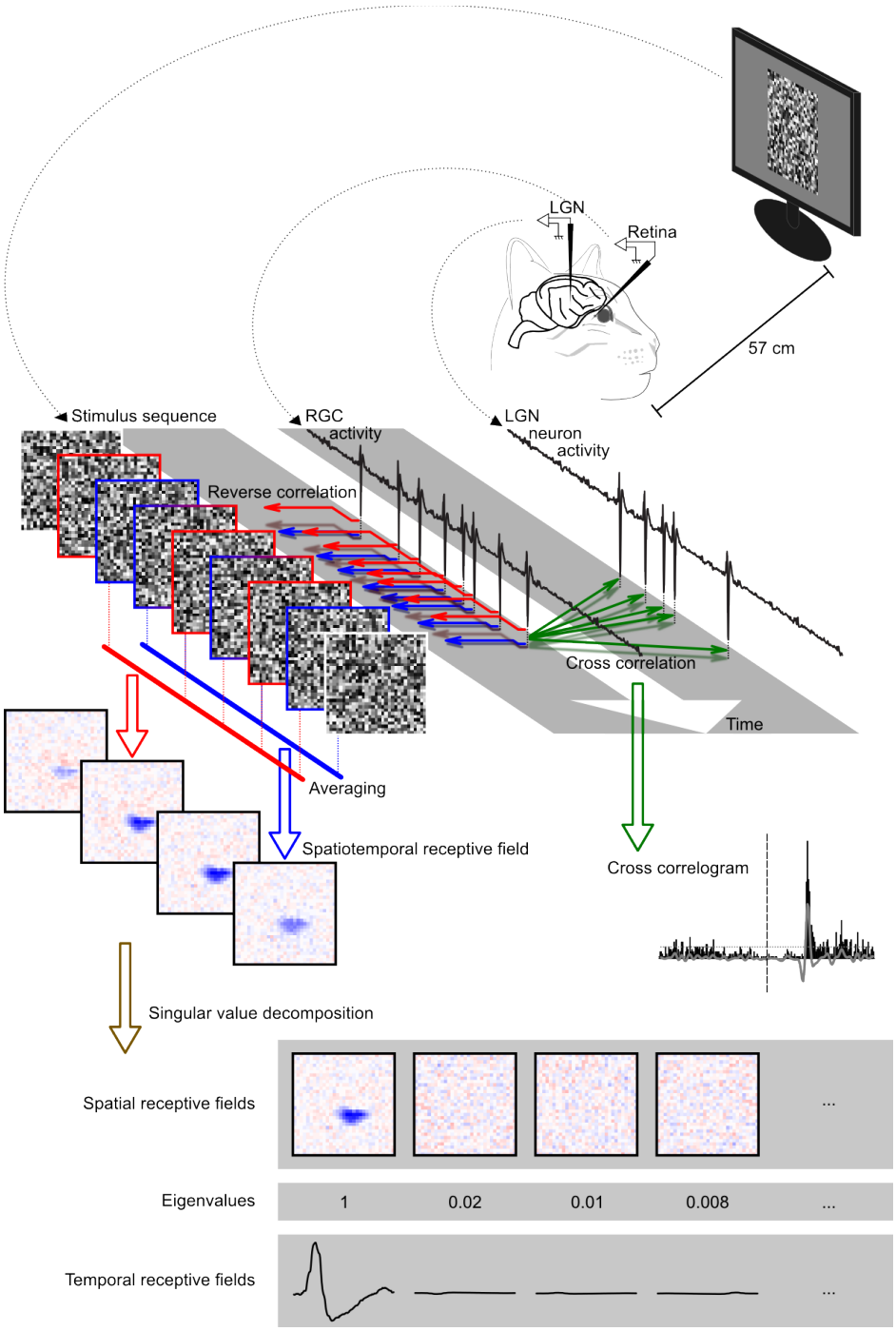

Figure 0.3: Experiment design (recording, reverse correlation, cross correlation, singular value decomposition).

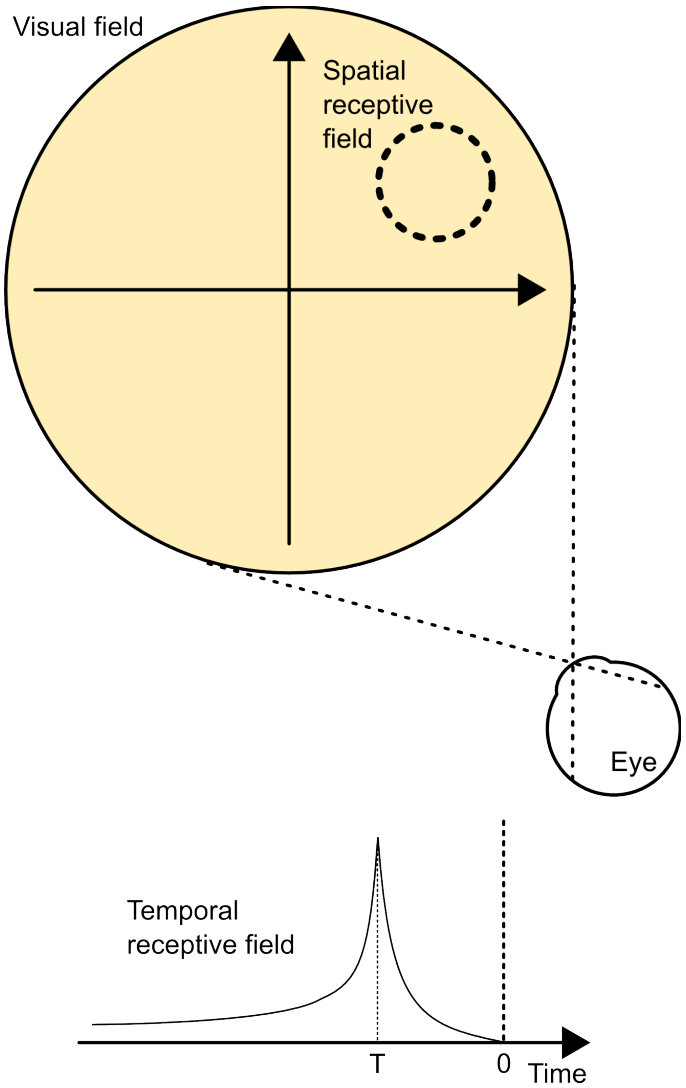

Figure 0.4: Schema of spatial and temporal RF. Spatial RF is the area at which a neuron is "looking". Temporal RF is, roughly, a response probability having temporal dynamics. This example neuron is activated T after the visual stimulus presentation on the upper-right part of the visual field.

References

Ahmed, B., and Hammond, P. (1991). Orientation bias of cat dorsal lateral geniculate cells: directional analysis of the major axis of the receptive field centre. *Exp. Brain Res*. 84, 676–9. doi: 10.1007/BF00230982.

Campbell, F., Cooper, G., and Enroth-Cugell, C. (1969). The spatial selectivity of the visual cells of the cat. *J. Physiol*. 203, 223–235.

Cheong, S. K., Tailby, C., Solomon, S. G., and Martin, P. R. (2013). Cortical-like receptive fields in the lateral geniculate nucleus of marmoset monkeys. *J. Neurosci*. 33, 6864–76. doi: 10.1523/JNEUROSCI.5208-12.2013.

Derrington, A. M., and Fuchs, A. F. (1979). Spatial and temporal properties of X and Y cells in the cat lateral geniculate nucleus. *J. Physiol*. 293, 347–364.

Enroth-Cugell, C., and Robson, J. G. (1966). The contrast sensitivity of retinal ganglion cells of the cat. *J. Physiol*. 187, 517–552.

Frishman, L. J., Freeman, A. W., Troy, J. B., Schweitzer-Tong, D. E., and Enroth-Cugell, C. (1987). Spatiotemporal frequency responses of cat retinal ganglion cells. *J. Gen. Physiol*. 89, 599–628. doi: 10.1085/jgp.89.4.599

Hubel, D. H., and Wiesel, T. N. (1959). Receptive fields of single neurones in the cat's striate cortex. *J. Physiol*. 148, 574–591.

Hubel, D. H., and Wiesel, T. N. (1962). Receptive fields, binocular interaction and functional architecture in the cat's visual cortex. *J. Physiol*. 160, 106–154.

Hubel, D. H., and Wiesel, T. N. (1977). Functional architecture of macaque monkey visual cortex. *Proc. R. Soc. Lond. B Biol. Sci*. 198, 1. doi: 10.1098/rspb.1977.0085

Movshon, J. A., Thompson, I. D., and Tolhurst, D. J. (1978). Spatial and temporal contrast sensitivity of neurones in areas 17 and 18 of the cat's visual cortex. *J. Physiol*. 283, 101–120.

Naito, T., Sadakane, O., Okamoto, M., and Sato, H. (2007). Orientation tuning of surround suppression in lateral geniculate nucleus and primary visual cortex of cat. *Neuroscience* 149, 962–75. doi: 10.1016/j.neuroscience.2007.08.001.

Niell, C. M. (2013). Vision: more than expected in the early visual system. *Curr. Biol*. 23, R681–4. doi: 10.1016/j.cub.2013.07.049.

Scholl, B., Tan, A. Y. Y., Corey, J., and Priebe, N. J. (2013). Emergence of orientation selectivity in the Mammalian visual pathway. *J. Neurosci*. 33, 10616–24. doi: 10.1523/JNEUROSCI.0404-13.2013.

Shou, T., and Leventhal, A. G. (1989). Organized arrangement of orientation-sensitive relay cells in the cat's dorsal lateral geniculate nucleus. *J. Neurosci*. 9, 4287–4302.

Sillito, A. M., Cudeiro, J., & Murphy, P. C. (1993). Orientation sensitive elements in the corticofugal influence on centre-surround interactions in the dorsal lateral geniculate nucleus. *Exp. Brain Res.* 93, 6-16.

Smith, E. L., Chino, Y. M., Ridder, W. H., Kitagawa, K., and Langston, A. (1990). Orientation bias of neurons in the lateral geniculate nucleus of macaque monkeys. *Vis. Neurosci*. 5, 525–45.

Soodak, R. E., Shapley, R. M., and Kaplan, E. (1987). Linear mechanism of orientation tuning in the retina and lateral geniculate nucleus of the cat. *J. Neurophysiol*. 58, 267–275.

Suematsu, N., Naito, T., and Sato, H. (2012). Relationship between orientation sensitivity and spatiotemporal receptive field structures of neurons in the cat lateral geniculate nucleus. *Neural Networks* 35, 10–20. doi: 10.1016/j.neunet.2012.06.008.

Suematsu, N., Naito, T., Miyoshi, T., Sawai, H., and Sato, H. (2013) Spatiotemporal receptive field structures in retinogeniculate connections of cat. *Front. Syst. Neurosci*. 7:103. doi: 10.3389/fnsys.2013.00103

Sun, C., Chen, X., Huang, L., & Shou, T. (2004). Orientation bias of the extraclassical receptive field of the relay cells in the cat's dorsal lateral geniculate nucleus. *Neuroscience*, 125, 495-505.

Zhao, X., Chen, H., Liu, X., and Cang, J. (2013). Orientation-selective responses in the mouse lateral geniculate nucleus. *J. Neurosci*. 33, 12751–63. doi: 10.1523/JNEUROSCI.0095-13.2013.

Theme 1

Relationship between orientation sensitivity and spatiotemporal receptive field structures of neurons in the cat lateral geniculate nucleus

Abstract

Although it is thought that orientation selectivity first emerges in the primary visual cortex, several studies have reported that neurons in the cat lateral geniculate nucleus (LGN) are sensitive to stimulus orientation, especially for high spatial frequency (SF) stimuli. To understand how this orientation sensitivity emerges, I investigated the spatiotemporal structures of linear receptive fields (RFs) of LGN neurons. Orientation tunings at several SFs were measured using sinusoidal drifting grating stimuli. Fine spatiotemporal structures of the linear RFs were measured using a reverse correlation technique and two-dimensional dynamic Gaussian white noise stimuli. A non-linear response modulation function was estimated by comparing measured responses with responses predicted from a linear RF structure. Although I found that a population of LGN neurons exhibited significantly elongated linear RF centers and that the angles of the long axes corresponded well to the preferred orientations, the orientation tunings predicted from the linear RFs were significantly broader than those measured. These results suggest that orientation-tuned non-linear response modulation induced by stimulation outside the classical RF contributes to the sharp orientation tuning seen in LGN neurons.

Introduction

Orientation selectivity is necessary for the detection of local edges in visual images and for the encoding of their orientations. For this reason, the principles of orientation selectivity are thought to describe how information is transformed in the early sensory system. It was originally thought that, at least in cats, orientation selectivity first appears in the receptive fields (RFs) of layer 4 neurons in the primary visual cortex (V1) upon receiving inputs from orientation insensitive lateral geniculate nucleus (LGN) cells (Hubel & Wiesel, 1959; Hubel & Wiesel, 1962).

Since then, however, several studies have reported that a certain population of neurons in the LGN can exhibit moderate orientation-biased responses to stimulations with high spatial frequency (SF) gratings (Soodak, Shapley, & Kaplan, 1987; Shou & Leventhal, 1989; Smith, Chino, Ridder, Kitagawa, & Langston, 1990). In these studies, the orientation-biased response is explained by an anisotropy that describes an elliptical classical receptive field (CRF) center that is thought to originate from retinal ganglion cells (Leventhal & Schall, 1983) based on the asymmetrical morphology of the dendritic field and orientation-biased responses to high SF gratings (Levick & Thibos, 1980; Soodak et al., 1987; Shou, Leventhal, Thompson, & Zhou, 1995).

In fact, by calculating the ellipticity of the CRF center from spatial frequency tunings in the preferred and orthogonal orientations using grating stimuli three times larger than the CRF, Soodak et al. (1987) argued that the orientation selectivity of LGN neurons arises directly from an elliptical CRF. More recent studies, however, have suggested that the non-linear response modulation from outside the CRF was sensitive to the stimulus orientation (Sillito, Cudeiro, & Murphy, 1993; Sun, Chen, Huang, & Shou, 2004; Naito, Sadakane, Okamoto, & Sato, 2007), suggesting an elliptical CRF alone does not explain orientation selectivity. It may be that the analysis by Soodak et al. (1987) already included

non-linear effects from outside the CRF, which could have resulted in overestimating the ellipticity of CRF. In other words, there still is a possibility that even when the CRF is completely circular, LGN neurons exhibit significant orientation selectivity due to a concomitant stimulation outside the CRF which induces orientation-sensitive surround suppression.

For this reason, I here directly describe the spatiotemporal RF structure of LGN neurons using a reverse correlation technique with dynamic Gaussian white noise stimuli. I found that a certain population of LGN neurons exhibits a significantly elongated CRF center and that the long axis of the CRF center of individual neurons corresponds to their preferred orientation. Additionally, the measured orientation tuning was significantly sharper than that predicted when using a linear RF. My results suggest that orientation-tuned non-linear operations between linear products from the CRF and spiking response may contribute to orientation tuning in the LGN and that this may be due to suppressive modulation elicited by stimulation outside the CRF.

Methods

All experimental protocols were approved by the Research Ethics Committee of Osaka University. All animal procedures were performed in accordance with the National Institute of Health Guidelines for the Care and Use of Laboratory Animals and the Guidelines of the Animal Care Committee of the Osaka University Medical School. All efforts were made to reduce the number of animals used.

Preparation

Three adult cats weighing 2.0–4.0 kg were used. Initially, atropine (0.1 mg, i.m.) was injected as premedication. Animals were anesthetized with a mixture of isoflurane (2–3%) and N_2O/O_2 (1:1). The trachea of each animal was intubated and a catheter was placed in the femoral vein. A local anesthetic, lidocaine (Xylocaine; AstraZeneca, Osaka, Japan), was administered at pressure points and around surgical incisions. The animals were then placed in a stereotaxic head holder, continuously paralyzed with pancuronium bromide (0.1 mg/kg/h, i.v.) to minimize eye movements, and maintained under artificial ventilation.

For craniotomy, lidocaine was carefully injected subcutaneously over the skull before cutting the skin. Before inserting a recording electrode, an opening was made in the skull, dura, and arachnoid above the LGN under anesthesia. The depth of anesthesia during this period was judged to be adequate because no significant heart rate change (>10%) was observed when the incision was made. During neuronal activity recording, isoflurane flow was stopped, a mixture of N_2O/O_2 (2:1) was supplied, and a mixed solution of fentanyl cirate (Fentanest; Sankyo, Tokyo, Japan; 0.1 ml/kg/h, i.v.), droperidol (Droleptan; Sankyo, 0.125 mg/kg/h, i.v.) and either Ringer's solution (Na^+ 147, K^+ 4, Ca^{2+} 4.5 and Cl^- 155.5 mEq/l) or high-K^+-concentration solution (Na^+ 35, K^+ 20, Ca^{2+} 35 and L-lactate 20 mEq/l) was

continuously infused through the femoral vein at 2 ml/kg/h. These two solutions were used alternately to adjust the blood electrolyte concentration. Sodium pentobarbital (2–4 mg/kg/h, i.v.) was added to the infusion solution when the animal's heart rate exceeded 240 beats/min or when it changed by more than 10% after the ear skin was firmly pressed with forceps. The nictitating membrane was retracted and the pupil was dilated with topical application of tropicamide (0.5%) and phenylephrine hydrochloride (0.5%) (Mydrin-P; Santen, Osaka, Japan). The eyes were refracted using O_2-permeable contact lenses with artificial pupils (4 mm in diameters) in order to focus them onto a cathode-ray tube (CRT) monitor. Rectal temperature was maintained at 37–38°C with a thermostatically controlled heating pad. The end-tidal CO_2 concentration was adjusted to 3.2–4%. An electroencephalogram, electrocardiogram, and heart rate were continuously monitored throughout the experiments.

Visual Stimulation and Recording Protocols

Extracellular single-unit recordings were made from cells in the LGN using tungsten-in-glass microelectrodes. All stimuli were generated using custom-made MATLAB (Mathworks, USA) programs with Psychtoolbox (Brainard, 1997; Pelli, 1997) and presented on a gamma-corrected CRT monitor (CPD-G500J, SONY; mean luminance, 70 cd/m^2; screen size, 40 × 30 cm^2; resolution, 1280 × 960 pixels; refresh rate, 100 Hz). Luminance linearity was confirmed within the experimental range. Electrophysiological signals were amplified and filtered (low and high cutoff frequencies were 300 and 5000 Hz, respectively) using an AC amplifier (Model 1800; AM Systems, USA) and sent to a spike sorter (Multi-Spike Detector; Alpha Omega Engineering, Nazareth, Israel), which performed on-line template matching of the action potentials. Digital pulses obtained by the template matching were acquired using a time-stamping board (Lisberger Tech., San Francisco, USA) at a sampling rate of 10 kHz. Single-unit action potentials were identified by the spike waveform with template matching. Neurons that exhibited monophasic spike waveforms were excluded from the analysis, because these

may include the axonal spiking activity of feedback projections from the cerebral cortex (Bishop, Burke, & Davis, 1962). Peristimulus time histograms (PSTHs) of unit responses were constructed and analyzed off-line.

To plot the CRF, an approximate center position of the CRF was first assessed by varying the spatial location of a small uniform patch stimulus whose diameter was usually less than 1 degree. I then presented two-dimensional dynamic dense white noise stimuli onto the approximated center position and conducted a reverse correlation to obtain an accurate center position from the obtained RF structure at peak response time.

SF (0.1–2.0 cycles/deg; 10 SFs equally spaced on a logarithmic axis) × orientation (0–337.5 deg; 16 orientations in 22.5 deg steps) tuning maps (SF×ORI maps) were measured using drifting sinusoidal gratings. I also measured spatial-summation tunings at preferred and orthogonal orientations. Cells were classified as either X- or Y-cells by employing commonly used criteria (Enroth-Cugell & Robson, 1966; Hochstein & Robert M Shapley, 1976; Bonin, Mante, & Carandini, 2005). The F1 component was used as the response magnitude for the drifting grating stimuli for both X- and Y-cells (Vidyasagar & Urbas, 1982; Sun et al., 2004; Naito et al., 2007). The optimal temporal frequency of a cell was measured by using large uniform patch stimuli (9.5 or 20 deg in diameter) that had temporally varied (0.5–32 Hz) polarities. The temporal frequency of all grating stimuli was adjusted to the cell's optimal frequency. Luminance contrast of stimulus was always 98%. For all neurons, I used a stimulus diameter sufficiently large to cover both the CRF and outside the CRF (9.5 or 20 deg in diameter). For a subpopulation of neurons, I also measured SF×ORI maps using small size gratings whose diameters were adjusted such that the gratings were inscribed inside the CRF center. The fine spatiotemporal structures of a linear RF were measured by a reverse correlation and two-dimensional dynamic dense

white noise stimuli as described above. To confirm that the linear RF structure was not altered over time, I measured the linear RF structures twice just after the each measurement of SF×ORI tuning maps for small and large size conditions. I usually used noise stimuli whose patch size was 9.5 × 9.5 degrees and a grid size of 0.16 × 0.16 or 0.31 × 0.31 degrees. To reconstruct the fine spatiotemporal linear RF structure, at least 1500 spikes (typically 3000–25000 spikes) were used.

An eye-hook from the stereotaxic apparatus was attached to one eye to fixate animal's head. To confirm that the astigmatism caused by the eye-hook did not affect the results, I compared orientation tunings, finding no systematic bias in preferred orientations or in the orientation selectivity index (OSI; see below for equation) between the two eyes.

To eliminate the possibility of multi-unit activities, I conducted the following. First, the presence of a refractory period was confirmed in the auto-correlogram of each neuron (Usrey, Alonso, & Reid, 2000; Okamoto, Naito, Sadakane, Osaki, & Sato, 2009). I also counted the number of spikes with interspike intervals less than 1 ms. If these exceeded 1% of the total spikes for a given cell during the entire recoding period, data for the cell were discarded (Okamoto et al., 2009). Finally, I used only the neurons whose waveforms were stable throughout the entire recording period.

I also took precautions to eliminate the possibility of recording feedback axonal activity from layer 6 of the visual cortex. For example, when using uniform circular stimuli (larger than 9.5 deg in diameter) in contrast-reversal modulation, most neurons exhibited their highest response at 8–16 Hz, they responded vigorously even at 32 Hz. Cortical neurons are unlikely to be able to do this (Ikeda & Wright, 1975; Movshon, Thompson, & Tolhurst, 1978; DeAngelis, Ohzawa, & Freeman, 1993). Furthermore, when roughly determining the CRF center position, I used small (less than 1 deg in

diameter, typically 0.5 deg in diameter) circular patch stimuli. Again, neurons responded vigorously. Because previous studies have reported that, unlike monkey V1, orientation selective neurons in the cat V1 have relatively large RFs (more than three times larger than CRF of LGN neurons; Naito et al., 2007; Ozeki, Finn, Schaffer, Miller, & Ferster, 2009), such small circular stimuli probably do not elicit the activity of cortical neurons. Finally, I discarded neurons that had monophasic spike waveforms, which may reflect putative axonal spiking activity (Bishop et al., 1962), to avoid recording any putative axonal spiking activity of feedback projections from the cortex.

Receptive Field Fitting

I fitted spatial RF structures at the peak response time with the following 12-parameter two-dimensional Gaussian function:

$$\text{Estimated RF} = a_e(G_c - a_s G_s) \qquad (1.1)$$

, where G_c and G_s are the center and surround Gaussians, respectively, and a_e and a_s are the amplitude of the response and the relative amplitude of the antagonistic surround, respectively. The Gaussians can be described as,

$$G_c = \exp[-(Z_c/\sigma_{Zc})^2 - (W_c/\sigma_{Wc})^2] \qquad (1.2)$$

$$G_s = \exp[-(Z_s/\sigma_{Zs})^2 - (W_s/\sigma_{Ws})^2] \qquad (1.3)$$

, where index c and s indicate the center and surround, respectively, and σ_Z and σ_W are the width of the Gaussian functions along the short (Z) and long axis (W), respectively. The W axis always corresponds to the RF long axis. In this fitting, each Gaussian function could elongate to a particular orientation. I

used the following functions for Z_c, Z_s, W_c, and W_s:

$$Z_c = -(X-X_c)\cos\theta_c-(Y-Y_c)\sin\theta_c \quad (1.4)$$

$$W_c = -(X-X_c)\sin\theta_c+(Y-Y_c)\cos\theta_c \quad (1.5)$$

$$Z_s = -(X-X_s)\cos\theta_s-(Y-Y_s)\sin\theta_s \quad (1.6)$$

$$W_s = -(X-X_s)\sin\theta_s+(Y-Y_s)\cos\theta_s \quad (1.7)$$

, where (X_c, Y_c) and (X_s, Y_s) are the mean center positions of the center and surround Gaussians. For fitting, I constrained $\sigma_Z \leq \sigma_W$. In practice, I used the MATLAB commands lsqcurvefit, which returns the estimated parameters, the squared 2-norm of the residual, and the Jacobian, and nlparci, which receives the output from lsqcurvefit and returns 95% confidence intervals for each parameter.

Orientation Tuning

The orientation tunings of a linear RF were computed by convolving the drifting gratings with the obtained linear spatiotemporal RF (0–150 ms or 0–200 ms in 1 ms steps). The measured orientation tunings were compared to the predicted tunings on the basis of the OSI by using the following equation:

$$OSI = \mathrm{sqrt}[\{\textstyle\sum_i R(\theta_i)\sin 2\theta_i\}^2+\{\sum_i R(\theta_i)\cos 2\theta_i\}^2]/\sum_i R(\theta_i) \quad (1.8)$$

, where $R(\theta_i)$ indicates the response (spikes/sec) for the i-th orientation θ_i (0–337.5 deg; 16 orientations in 22.5 deg steps). The OSI takes values between 0 and 1: an OSI = 0 indicates that the neuron responds equally to all orientations and an OSI = 1 indicates that the neuron responds to only one orientation. An OSI $\geq$ 0.1 was considered significant (Batschelet, 1981; Leventhal & Schall, 1983; Zar, 1996; Sun et al., 2004).

Response Prediction from the Linear Receptive Field

Although there are several ways to predict neural responses to visual stimuli from the spatiotemporal structure of a linear RF, I predicted neural responses by convolving the stimuli with the spatiotemporal structure (Dan, Atick, & Reid, 1996; Anzai, Ohzawa, & Freeman, 1999; Bonin et al., 2005).

To investigate whether the spatiotemporal structure of the linear RF of individual LGN neurons can explain their orientation selectivity, I computed linear response predictions by convolving drifting grating stimuli with the spatiotemporal structure of the linear RF (predicted PSTH) followed by half-rectifying the predicted PSTH. The predicted PSTH at time t is computed as follows:

$$\text{Predicted PSTH}(t) = \sum_{\tau=0,\,m} \langle L(\tau) \mid S(t-\tau) \rangle \quad (1.9)$$

, where L and S indicate two-dimensional spatial structures of the linear RF and drifting grating stimulus, respectively, and $\langle \cdots \mid \cdots \rangle$ represents the inner product of two vectors. The index m is the temporal length of the linear RF (150 or 200).

The linear response prediction is given by the half-rectification of the predicted PSTH.

$$\text{Linear response prediction}(t) = \max[\text{Predicted PSTH}(t), 0] \quad (1.10)$$

, where max[⋯] is the "MAX" operator. I obtained the predicted SF×ORI map by conducting operations Equations 1.9 and 1.10 for each drifting grating stimuli parameter and calculated the F1 components of

the linear response predictions. Measured and predicted F1 components were compared for both X- and Y-cells.

It is also possible to obtain a response prediction from the 2D Fourier transform of the RF (Gardner, Anzai, Ohzawa, & Freeman, 1999), which is mathematically similar to my method. However, as I describe below, to estimate the non-linear response modulation function, I used previously described methods (Anzai et al., 1999; Chichilnisky, 2001; Solomon, Tailby, Cheong, & Camp, 2010), which are better suited to my above analysis.

Static Non-linear Response Modulation Function

I compared the measured PSTH with the predicted PSTH to estimate the non-linear response modulation function (Anzai et al., 1999; Chichilnisky, 2001; Solomon et al., 2010). PSTHs were convolved with a rectangular function of 40 ms width and zero-padding. The sliding time was 1 ms, giving mean spike counts in each overlapping 40-ms-bin. Finally, I plotted the measured PSTH as a function of the predicted PSTH in each corresponding time bin (gray filled circles in Figure 1.7), resulting in a static non-linear response modulation function that can be described by the following power function:

$$Y = A \max[X-\theta, 0]^n+b \quad (1.11)$$

, where Y and X indicate the measured spike count and the predicted response value, respectively. A, θ, n, and b indicate the amplitude, threshold, exponent, and baseline of the non-linear response modulation function, respectively. When n is 1, the relationship between Y and X is linear for $X > \theta$ (half-rectification), while the function is expansive for $n > 1$ and compressive for $n < 1$. The linear

prediction assumes $\theta = 0$, $n = 1$, and $b = 0$.

For $X > \theta$, I divided X values into ten equally spaced bins and calculated the mean X and Y values in each bin (open circles in Figure 1.7). To estimate the degree of the non-linear response modulation, I fitted the power function (Equation 1.11) to these mean data points by fixing θ to 0 and b to the minimum mean value. This allowed me to solve for n and A. Because for most neurons orientation tunings at the high SF for the large size condition were less accurately predicted from the linear RF than the optimal SF, I compared the non-linear response modulation in the preferred orientation with that in the orthogonal orientation at high and optimal SFs and for large and small size conditions.

Histology

At the end of each penetration, at least three electrolytic lesions were made along the track by passing a current (DC, 3–4 μA, 10 sec, tip negative). Lesions were separated by intervals of more than 300 μm. After the recording experiments, the animals were deeply anesthetized with sodium pentobarbital (60 mg/kg, i.v.) and perfused transcardially with buffered saline (pH 7.4) followed by 4% paraformaldehyde in 0.1 M phosphate-buffered saline (PBS). Blocks of the dorsolateral thalamus were obtained and immersed in 30% sucrose in PBS for 36–48 h. Eighty-micrometer-thick frozen coronal sections were sliced on a microtome and kept in PBS. Sections were stained for cytochrome oxidase. The laminar locations of the recording sites were then identified under a light microscope. Shrunk thalamic tissues were corrected for by multiplying the ratio of the measured lesion distance by the value calculated from the micrometer reading. LGN layers were classified into layers A, A1 and C.

Results

I recorded 55 LGN neurons (Layer A = 28, A1 = 23, C = 4; X = 45, Y = 7, unknown = 3; On-center = 29, Off-center = 26; eccentricity, 0.9–39.6 deg, mean = 13.8 deg, median = 8.9 deg) from three adult cats, measured the orientation tunings, and compared these with linear predictions from spatiotemporal RF structures made by a reverse correlation technique using Gaussian white noise stimuli.

SF×ORI Map and Orientation Tunings of LGN Neurons

An SF×ORI map of the 55 LGN neurons was made by using drifting sinusoidal gratings of 10 SFs (0.1–2.0 cycles/deg, equally spaced on a logarithmic axis) and 16 orientations (0–337.5 deg, in 22.5 deg steps). The temporal frequency of the gratings was adjusted to the cell's optimal frequency. For all neurons, the diameter of the grating was 9.5 or 20.0 deg (large size condition), which fully covered both the CRF and outside the CRF (Bonin et al., 2005; Naito et al., 2007). For 38 of the 55 neurons, I also measured another SF×ORI map using smaller size gratings at which the grating diameter was adjusted to equal the width of the linear CRF center (small size condition) to eliminate non-linear suppressive surround effects (Bonin et al., 2005; Naito et al., 2007), since the orientation selectivity of LGN neurons depends not only on the SF but also on the stimulus size (Naito, Osaki, Sadakane, Okamoto, Shimegi, & Sato, 2009). A typical SF×ORI map of an X-LGN neuron is shown in Figure 1.1A.

The degree of orientation selectivity for each neuron was evaluated by calculating the OSI, which is a global measure for tuning across the entire tuning curve, at three different SFs. The optimal SF was defined as the SF at which neurons exhibited maximum responses, while high and low SFs were defined as the highest and lowest SFs, respectively, at which the response of the neuron was more than 50% that at optimal SF.

Figure 1.1B shows orientation tunings for the large and small size conditions at low, optimal and high SFs. This neuron exhibits relatively broad orientation tunings for the small size independent of SF (dashed lines with open circles; OSI at low, optimal, and high SF were 0.05, 0.07, and 0.15, respectively), but sharper orientation tunings for the large size, especially at the high SF (solid lines with filled circles; OSI at low, optimal, and high SF were 0.14, 0.24, and 0.39, respectively).

Figure 1.1C shows the distribution of OSIs for both sizes (N = 55 and 38 for large and small, respectively). When large size stimuli with the high SF were used, 44 of the 55 neurons exhibited significant orientation selectivity (OSI $\geq$ 0.1) (Figure 1.1C, top-right) with a mean OSI significantly greater than 0.1 (mean OSI = 0.25, t-test, $p < 0.0001$). However, in all other conditions, the mean OSI was not significantly larger than 0.1 (mean OSI for the large size at the low SF, large size at the optimal SF, small size at the low SF, small size at the optimal SF, and small size at high SF = 0.06, 0.08, 0.04, 0.04, and 0.1, respectively; t-test, p = 1.0, 0.94, 1.0, 1.0, and 0.22, respectively). There was a weak correlation between the eccentricity of RF and OSI ($r = 0.21$, $p = 0.06$). In short, LGN neurons usually exhibited sharp orientation tunings when a high SF and large size grating stimuli were presented.

Figure 1.1D shows the distribution of preferred orientations measured with large size drifting grating stimuli with high SF. For the 55 neurons, population of neurons exhibited the preferred orientation near 90° corresponding to the horizontal orientation. The distribution was significantly different from uniform (v-test, $p < 0.05$). This result is consistent with the so-called "oblique effect" reported in the neurons in area 17 (Li, Peterson & Freeman, 2003; Shen, Liang & Shou, 2008) and 21a (Huang, Shou, Chen, Yu, Sun & Liang, 2006) of cat. I also found that there was a significant positive correlation between the preferred orientation and eccentric angle, that refers the angles between a

vertical axis and a line connecting an RF center position with an *area centralis* (data not shown, correlation coefficient, $r = 0.88$, $p < 0.01$).

Predicted Orientation Tunings from a Linear Receptive Field

To examine how well the orientation tunings predicted from the linear RF can explain the measured tunings, I mapped the spatiotemporal structure of the linear RF using a reverse correlation technique for each neuron. A typical example of an X-cell at peak response time is shown in Figure 1.2A. The measured linear RF center was slightly elongated along the vertical orientation. To estimate the orientation of its long axis, the RF was fitted with a two-dimensional Gaussian function (Equation 1.1; see Methods). To evaluate the ellipticity of the linear RF center, the aspect ratio (long axis/short axis) of the CRF center was calculated from the fitted linear RF (see Methods). When the 95% confidence interval of the aspect ratio did not overlap with a ratio = 1, the RF was considered significantly elongated. Figure 1.2B shows the distribution of aspect ratios for the fitted linear RF center (N = 55). Filled and hatched bars indicate the number of neurons with significantly (46 neurons) and not significantly (9 neurons) elongated RF centers, respectively (N = 55, mean aspect ratio = 1.62 ± 0.57 SD). Figure 1.2C depicts the relationship between the angle of the linear RF center's long axis and the preferred orientation, which was calculated from the measured orientation tuning at high SF. When the 95% confidence interval of the estimated angle of the long axis of the linear RF did not overlap with that of the preferred orientation calculated from the orientation tuning, the long axis was considered to be significantly different from the cell's preferred orientation. Among the 46 neurons with significantly elongated RFs, the long axis orientations of the majority (26/46) did not differ from the preferred orientations measured when using drifting gratings (Figure 1.2C). Also, the mean absolute difference in orientations for all neurons (N = 55, 18.4° ± 21.2 SD) was small. This suggests that the long axis of the elliptical CRF center of LGN neurons essentially corresponds to its preferred orientation. There was a

significant positive correlation between eccentricity and aspect ratio of RF (r = 0.23, p < 0.05), suggesting that neurons with peripheral RF tended to show more elongated RF.

To investigate whether the elliptical CRF center can explain the orientation tunings of LGN neurons, I computed linear predictions of the SF×ORI maps by convolving the stimulus and the linear RF (Equation 1.10; see Methods). Figure 1.3 shows the measured and predicted SF×ORI maps of an X-cell for small (Figure 1.3A) and large size conditions (Figure 1.3B). While the linear prediction for the small size condition captured well the measured SF×ORI map (Pearson product-moment correlation coefficient, r = 0.99), this was not true for the large size condition. That is, unlike the measured tuning map for which there was a substantial response, in the predicted tuning map there was no response in the parameter area for cross-orientation at low SFs. The correlation coefficient of the maps for the large size condition was 0.87. For population analysis, I compared correlation coefficients between the two stimulus sizes (Figure 1.3C, N = 38), finding the correlation coefficient for the large size condition was significantly smaller than that for the small size one (mean r for large and small size conditions = 0.68 and 0.82; paired t-test, p < 0.0005). The linear response of the CRF fails significantly more to predict the tunings in the large size than the small size condition.

The poorer prediction accuracy of the large size condition may be due to a lower firing rate which causes a higher coefficient of variation. I therefore compared the firing rates of the two size conditions. No significant difference was found (N = 38; mean firing rates for large and small size conditions = 38 ± 24SD and 39 ± 27SD spikes/sec, respectively; paired t-test, p = 0.59). This is because the diameter of the small size grating was adjusted to the length of the short axis of the linear RF to avoid contamination by non-linear surround effects (see Methods).

Figure 1.4A shows a typical example of a comparison of orientation tuning curves from measured RF and predicted linear RF responses of an X-cell for the large size condition. The neuron exhibits sharp orientation tuning at the high SF (right, solid line with filled circles, OSI = 0.43), while the predicted tuning was slightly broad (right, dashed line with open circles, OSI = 0.28). In contrast, at the low SF (Figure 1.4A, left), the result was opposite (measured and predicted OSIs = 0.062 and 0.092, respectively). That is, the linear prediction for the low SF overestimated the OSI. At the optimal SF (Figure 1.4A, middle), the measured and predicted orientation tunings were very similar to each other (measured and predicted OSIs = 0.14 and 0.15, respectively). Figure 1.4B shows OSI scatter charts for each SF for 55 cells. At the high SF (Figure 1.4B, right), most data points were distributed under the diagonal line, indicating the prediction underestimated orientation selectivity (Welch's t-test, $p < 0.001$). In contrast, at the low SF (Figure 1.4B, left), the prediction significantly overestimated the orientation selectivity (Welch's t-test, $p < 0.0005$). At the optimal SF (Figure 1.4B, middle), there was no significant difference between the two OSIs (Welch's t-test, $p = 0.07$).

In short, orientation tuning at the optimal SF was relatively well predicted, while those at low and high SFs were not. There are at least two possible explanations for these results, one technical and one biological. Technically, the grid size of the white noise stimuli may have been inadequately fine for predicting neuronal responses to gratings with non-optimal spatial frequencies. Biologically, there may exist non-linear response modulations in the LGN neuron responses. I address these possibilities below.

Incidentally, for the large size condition, I compared the prediction accuracies between ON- and OFF-center cells and between X- and Y-cells. There was no significant difference between the ON- and OFF-center cells (mean r of ON- and OFF-center cells = 0.72 and 0.74, respectively; Welch's t-test, $p = 0.76$), whereas the prediction accuracy of the Y-cells was significantly higher than that of the X-cells (mean r for X- and Y-cells = 0.71 and 0.86, respectively; Welch's t-test, $p < 0.005$). However, because

my population includes only a small number of Y-cells (N = 7), conclusions are limited.

Grid Size Effect on Predictions

Allen & Freeman (2006) have noted that the grid size of noise stimuli could affect the response prediction, which could risk underestimating the antagonistic surround of the CRF, especially at low SFs. While finer noise patches could provide spatially high-resolution RF structures, they elicit less vigorous responses, resulting in an underestimate of the antagonistic surround of the CRF because the stimulation intensity of fine noise in a large area frequently equals the background (gray) level. Coarser noise can mitigate this problem, but also results in linear RF structures of spatially low-resolution.

One possible explanation for my observed overestimation of orientation tunings at the low SF may be the effects of the antagonistic surround stimulation within the CRF were underestimated. When the CRF of an LGN neuron has antagonistic surround elongated to the same orientation as the CRF center, responses to CRF center stimulation in the preferred orientation at low SFs may be strongly suppressed. On the other hand, the effect is only weak in the orthogonal orientation because of the elliptical shape of the antagonistic CRF surround.

I therefore examined grid size effects on the prediction accuracy. First, I measured the spatiotemporal structure of a linear RF (low-resolution RF) using coarse noise stimuli whose grid size was typically 0.31 × 0.31 or 0.63 × 0.63 degrees, which is two or three times larger than that of fine ones, and predicted the SF×ORI tuning maps with a low-resolution RF for 23 neurons. Figure 1.5A illustrates a representative difference in linear RFs between different grid size conditions (left, high-resolution linear RF; right, low-resolution linear RF). When a coarse white noise stimulus was used, most LGN neurons exhibited more prominent CRF surround than those measured with fine grid

size noise (bluish region surrounding the reddish CRF center).

Figure 1.5B shows predicted SF×ORI maps with high- (left) and low-resolution linear RFs (right). Because this neuron had a slightly elongated antagonistic CRF surround along the long axis of the CRF center, the predicted orientation tuning at the low SF became broader.

I also compared correlation coefficients between measured and predicted SF×ORI maps with low- and high-resolution RFs (Figure 1.5C, N = 23), finding no significant difference between the conditions (two-tailed paired t-test, $p = 0.16$). The prediction accuracies for the two RF conditions were equally similar.

I then compared measured OSIs and predicted OSIs calculated from the predicted SF×ORI map obtained at a low-resolution RF at low, optimal and high SFs (Figure 1.6, N = 23). There was no significant difference between measured and predicted OSIs at the low SF (Figure 1.6, left; paired t-test, $p = 0.26$), suggesting that the overestimated orientation tuning (Figure 1.4B, leftmost) may be the result of underestimating the antagonistic CRF surround. The optimal SF (Figure 1.6, middle) also showed no significant difference between the measured and predicted OSIs (paired t-test, $p = 0.78$). However, at the high SF (Figure 1.6, right), the predicted orientation tunings remained significantly broader than the measured ones (paired t-test, $p < 0.0005$), which were slightly broader than those seen at the high-resolution RF (mean OSI at the high SF from the low-resolution and high-resolution RFs were 0.15 and 0.16, respectively). These results suggest that low-resolution RFs may provide better tuning prediction at low SFs, but worse tuning prediction at high SFs, which therefore may explain why prediction accuracies of high- and low-resolution RFs across all SFs were almost identical (Figure 1.5C).

Static Non-linear Response Modulation Function

Above I suggest non-linear response modulation contributes to the poor linear prediction of orientation tunings under a large stimulus size with high SFs. To further investigate this, I computed a static non-linear response modulation function that was based on a linear-non-linear cascade model (Anzai et al., 1999; Chichilnisky, 2001; Solomon et al., 2010) (see Methods). Figure 1.7 shows a representative example of the non-linear response modulation function estimated from responses to drifting gratings. Filled gray circles indicate the predicted response value (X-axis) in a particular time bin and the measured spike count (Y-axis) in the corresponding time bin. For X > 0, X values were first divided into ten equally spaced bins, followed by calculating the mean X and Y values in each bin (open circles), and finally fitting Equation 1.11 (see Methods) to these means. This resulted in an n (exponent) and A (amplitude) of 0.51 and 60, respectively.

I then compared n and A between preferred and orthogonal orientations and between large and small size conditions (N = 55 and 38, respectively) (Figure 1.8A–D). For the small size condition (Figure 1.8A and B, open circles), n was approximately 1 for all SFs and orientations (optimal SF in the preferred orientation, mean n = 1.0, t-test, H_0: mean n = 1, H_1: mean $n \neq 1$, p = 0.98; optimal SF in the orthogonal orientation, mean n = 0.84, p = 0.13; high SF in the preferred orientation, mean n = 0.95, p = 0.65; and high SF in the orthogonal orientation, mean n = 0.82, $p < 0.05$). For the large size condition, LGN neurons often exhibited a non-linear response modulation function whose n was significantly smaller than 1 (Figure 1.8A and B, filled circles; optimal SF in the preferred orientation, mean n = 0.57, t-test, H_0: mean n = 1, H_1: mean $n < 1$, $p < 0.005$; optimal SF in the orthogonal orientation, mean n = 0.62, $p < 0.005$; high SF in the preferred orientation, mean n = 0.61, $p < 0.005$; high SF in the orthogonal orientation, mean n = 0.53, $p < 0.005$), suggesting that the non-linear response modulation was compressive. This may be because I always used drifting grating stimuli with high luminance contrast

(Bonin et al., 2005; Duong & Freeman, 2008). These results are consistent with my findings that the SF×ORI tunings for the small size condition were well predicted from the linear RF, while those for the large size condition were not (Figure 1.3).

At the optimal SF (Figure 1.8A and C), there were no significant differences in n and A between the two orientations. However, n in the preferred orientation for the large size condition was significantly smaller than that for the small size (mean n for large and small size conditions = 0.57 and 1.0, respectively; Welch's t-test, $p < 0.005$). Although a similar tendency was observed in the orthogonal orientation, the difference was not significant (mean n for large and small size conditions = 0.62 and 0.84, respectively; Welch's t-test, $p = 0.067$). In other words, there was a size dependency for n in the preferred orientation only.

At high SF (Figure 1.8B and D), there were clear size effects on n in both orientations (mean n in the preferred orientation for large and small size conditions = 0.61 and 0.95, respectively, Welch's t-test, $p < 0.01$; those in the orthogonal orientation = 0.53 and 0.82, respectively, Welch's t-test, $p < 0.005$). Additionally, at the high SF for the large size condition, there was a clear orientation dependency in A (mean A in the preferred and orthogonal orientations = 53 and 38, respectively; paired t-test, $p < 0.01$). In contrast, for the small size condition, neither n nor A showed dependency on orientation (open circles).

These results indicate that a substantial proportion of the non-linear response modulation originates from outside the CRF. This orientation-tuned non-linear response modulation will make neurons less active in the orthogonal orientation than in the preferred orientation at high SFs by decreasing n in both orientations, but A in the orthogonal orientation only.

Finally, I recomputed OSIs at a high SF for large size grating stimuli from the non-linear response modulation of linear predictions (LNOSIs). Comparisons to measured OSIs (Figure 1.8E) showed no significant difference (mean LNOSI and measured OSI = 0.22 and 0.25, paired t-test, p = 0.089). However, LNOSIs were significantly larger than OSIs predicted from linear RFs (LOSIs) (mean LOSI = 0.17, paired t-test, $p < 0.005$). Although at the high SF in the preferred orientation the A of Y-cells was significantly higher than that of X-cells (mean A of X- and Y-cell = 49 and 76, respectively; Welch's t-test, $p < 0.05$), there was no significant difference between X- and Y-cell LNOSIs (mean LNOSIs of X- and Y-cells = 0.22 and 0.18, respectively; Welch's t-test, p = 0.29), between the X-cell measured OSI and LNOSI (mean measured OSI of X-cell = 0.25; paired t-test, p = 0.071), and between the Y-cell measured OSI and LNOSI (mean measured OSI of Y-cells = 0.23; paired t-test, p = 0.36). These results indicate that both an elongated linear RF and non-linear response modulation are necessary to generate the high-SF-tuned orientation tunings in X- and Y- LGN neurons.

Discussions

In the present study, 44 of 55 (80%) observed LGN neurons exhibited significant orientation sensitivity when the CRF and outside the CRF were stimulated with a large size stimulus of a high SF. Other studies have also reported a comparable abundance ratio for LGN neurons. For example, 81% of LGN neurons were found to exhibit orientation selectivity in response to thin, long bar stimuli (Vidyasagar & Urbas, 1982), 90% to sinusoidal drifting gratings with high SFs and at least three times as large as the RF center (Shou & Leventhal, 1989), and 69% when stimulating the CRF and outside the CRF separately with optimal SF gratings (Sun et al., 2004).

Furthermore, 46 neurons in the present study had significantly elongated linear RF centers, as determined by the reverse correlation technique (Figure 1.2B). For 20 of these, the angles of the long axis were significantly, but only slightly, different from the preferred orientations (Figure 1.2C). Overall, I interpreted these results to mean the elliptical CRF center may be a source for orientation tuning in the LGN.

However, the elliptical RF is not sufficient to explain the entire orientation tuning for a large size stimulus with high SF gratings. In this condition, the predicted orientation tuning was significantly broader than the measured one. Furthermore, I found non-linear response modulation made a significant contribution to the observed sharp orientation tuning of LGN neurons. The similar effect of non-linear response modulation from outside the CRF on orientation tuning has been reported in V1 (Henry, Bishop & Dreher, 1974; Henry, Dreher & Bishop, 1974, Henrie & Shapley, 2001; Chen, Dan & Li, 2005; Okamoto et al., 2009).

I calculated two parameters of the non-linear modulation, n and A (see Equation 1.11). n was

significantly smaller than 1 for all orientations at the large size condition and was not sensitive to the orientation (Figure 1.8A and B), suggesting non-orientation-tuned compressive modulation from outside the CRF. This is in agreement with the results of Bonin et al. (2005), which suggest *n* might be equivalent to a non-linear response modulation generated by surround suppression.

Additionally, I found the non-linear response modulation component *A* can enhance orientation tuning strongly because of its orientation selectivity, which is significantly stronger for the short axis than for the long axis of the linear RF for large size gratings with high SFs (Figure 1.8D), suggesting *A* plays a significant role in generating the sharp orientation tuning of LGN neurons. Bonin et al. (2005) may have failed to detect *A*, because they used only one prefixed orientation for the center grating stimulus (see Naito et al., 2007).

Two Possible Mechanisms for an Elongated Classical Receptive Field

I considered two possible mechanisms that could lead to the above elliptical RFs. One is a dendritic arborization bias in retinal ganglion cells. Leventhal & Schall (1983) reported that most retinal ganglion cells in cats have elliptically extended dendrites with a mode in their aspect ratio (or "axes ratio"), which provides a measure of the elongation of each dendritic field (1.10–1.20). I found a distribution of the CRF center aspect ratio (Figure 1.2B; N = 55, mean = 1.62 ± 0.57 SD, median = 1.44) that was similar but slightly longer than their results, suggesting a distortion in retinal ganglion cell dendrites likely causes the elliptical CRF in LGN neurons, although other processes may also contribute. The second mechanism I considered is that the projection from a retinal ganglion cell to LGN neuron is not one-to-one. Instead, retinal ganglion cells that have CRFs spatially in-line with each other may converge to one LGN neuron. By observing that the CRFs of immature and adult ferret LGN neurons are elongated (mean aspect ratios = 2.0 and 1.62, respectively), Tavazoie & Reid (2000) proposed a

convergence/divergence model for thalamocortical development where converging inputs from a number of retinal ganglion cells to LGN neurons enlarge geniculate CRFs during early thalamocortical development and divergent inputs from the retina to the LGN are more common at later developmental stages, causing some geniculate CRFs to become less elliptical. It is possible that a similar mechanism works in cat retinothalamic projections.

Origin of the Non-linear Response Modulation

Although I found that a population of LGN neurons exhibited significantly elongated CRF centers and that their long axis most often corresponded to the neuron's preferred orientation, the degree of orientation selectivity could not be completely explained by the ellipticity. Rather, my results show that orientation-tuned non-linear response modulation is also important in generating sharp orientation tuning in the LGN. The non-linear response modulation was compressive (suppressive), especially in response to high SF grating stimuli in the orthogonal orientation. In addition, this non-linear response modulation was dependent on stimulus size, suggesting that the non-linear response modulation is generated by orientation-sensitive surround suppression (Sillito et al., 1993; Jones, Andolina, Oakely, Murphy, & Sillito, 2000; Sun et al., 2004; Naito et al., 2007).

From where does the orientation- and size-dependent non-linear response modulation originate? One possibility is that the non-linear response modulation already exists in inputs from retinal ganglion cells. Girman & Lund (2010) reported that a significant number of rat retinal ganglion cells exhibit significant orientation-dependent modulation of the center response by surround stimulation, while Nolt et al. (2007) studied the degree of suppression at high SF in the LGN of cat with S-potentials and showed that suppression at high SF can originate from retinal inputs even if the suppression in the LGN is stronger than that in the retinal inputs. Alitto & Usrey (2008) reported that extraclassical suppression

in macaque retinal inputs is comparable to that in the LGN and that it originates too quickly to involve corticothalamic feedback. Although suppression in cat retinal input appears to make less contribution than that of macaque, it still acts as a considerable source for non-linear response modulation.

Another possible source for the inhibitory feedback projection is from the cortex via local interneurons in the LGN and/or thalamic reticular nucleus. For example, Nolt et al. (2007) showed that part of high-SF-tuned surround suppression is abolished by cortical cooling, concluding about one quarter of the high-SF-tuned suppression originates from corticothalamic feedback.

In general, simple cells in the adult cat striate cortex are more tuned to higher SFs (mean optimal SF = 0.42 cycles/deg, DeAngelis et al., 1993) than LGN neurons (mean optimal SF = 0.34 cycles/deg from the present study, data not shown). This may account for the non-linear response modulation, especially when activated by SFs higher than optimal for the CRF center. Neuropharmacologically speaking, previous work has found that orientation sensitivity in the LGN becomes weaker under iontophoretic administration of bicuculline, a GABAa receptor antagonist, at high contrast conditions (Naito et al., 2009), suggesting local GABAa inhibition is a possible source for the non-linear response modulation.

The Functional Significance of Orientation-tuned Non-linear Response Modulation

In the present study, I found that most LGN neurons have elliptical, not circular, CRF centers. These elliptical CRF centers, in combination with orientation-tuned surround suppression, may contribute to sharp orientation tuning in the LGN. It is expected that orientation tuning induced only by an elliptical CRF center will vary depending on the luminance contrast of the stimulus. Because there exists a spiking response threshold, some may argue the tuning bandwidth of the orientation tuning

caused by an elliptical CRF center should become broader as the stimulus contrast increases, a phenomenon known as "the iceberg effect" (Sompolinsky & Shapley, 1997; Carandini & Ferster, 2000; Volgushev, Pernberg, & Eysel, 2000). However, I have found that orientation tuning of cat LGN neurons is contrast invariant, such that as contrast increases the non-linear suppression becomes stronger at orthogonal orientations to maintain sharp orientation tuning of LGN neurons at high contrast conditions (Naito et al., 2009). This suggests that the orientation tuning caused by an elliptical CRF center and by orientation-tuned suppression is well designed for responding to varying stimuli.

In addition, I found that the largest number of LGN neurons had preferred orientations around 90 deg, perhaps related to the "oblique effect" mainly observed in V1. This result suggests that V1 neurons take preferred orientations from LGN neurons, and therefore the "oblique effect" was observed in both LGN and V1.

Figures

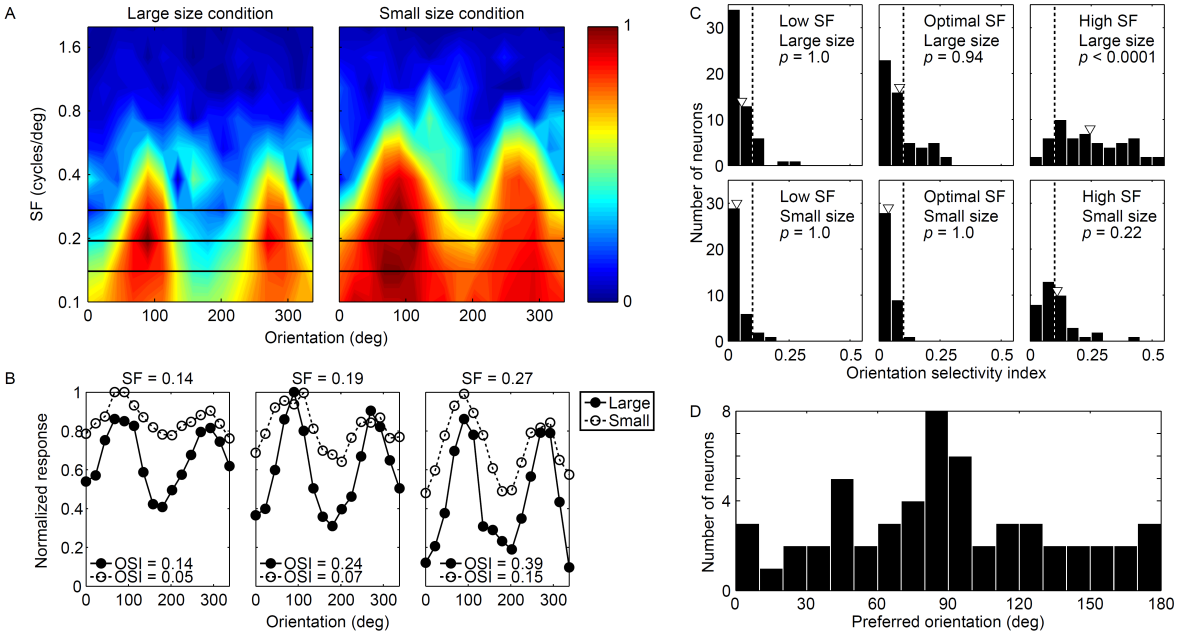

Figure 1.1: Distribution of the orientation selectivity index (OSI) measured from SF×ORI maps. A) Examples of SF×ORI maps for large and small size conditions. X- and logarithmic Y-axes indicate orientation and SF, respectively. The color bar indicates the strength of the response to the grating stimuli with red being strongest. The three horizontal solid lines in each map indicate the high, optimal, and low SFs referred to in B. B) Orientation tuning curves at each SF. Solid lines with filled circles and dashed lines with open circles indicate large and small size conditions, respectively. C) OSI distributions at low, optimal and high SFs for large and small size conditions. Open arrowheads indicate mean OSIs. Vertical dashed lines indicate the minimum OSI for significance (OSI = 0.1). P-values were obtained from t-tests, H_0: mean OSI = 0.1, H_1: mean OSI > 0.1. D) The distribution of preferred orientations measured with large size and high SF drifting gratings. Most data are distributed around 90 deg.

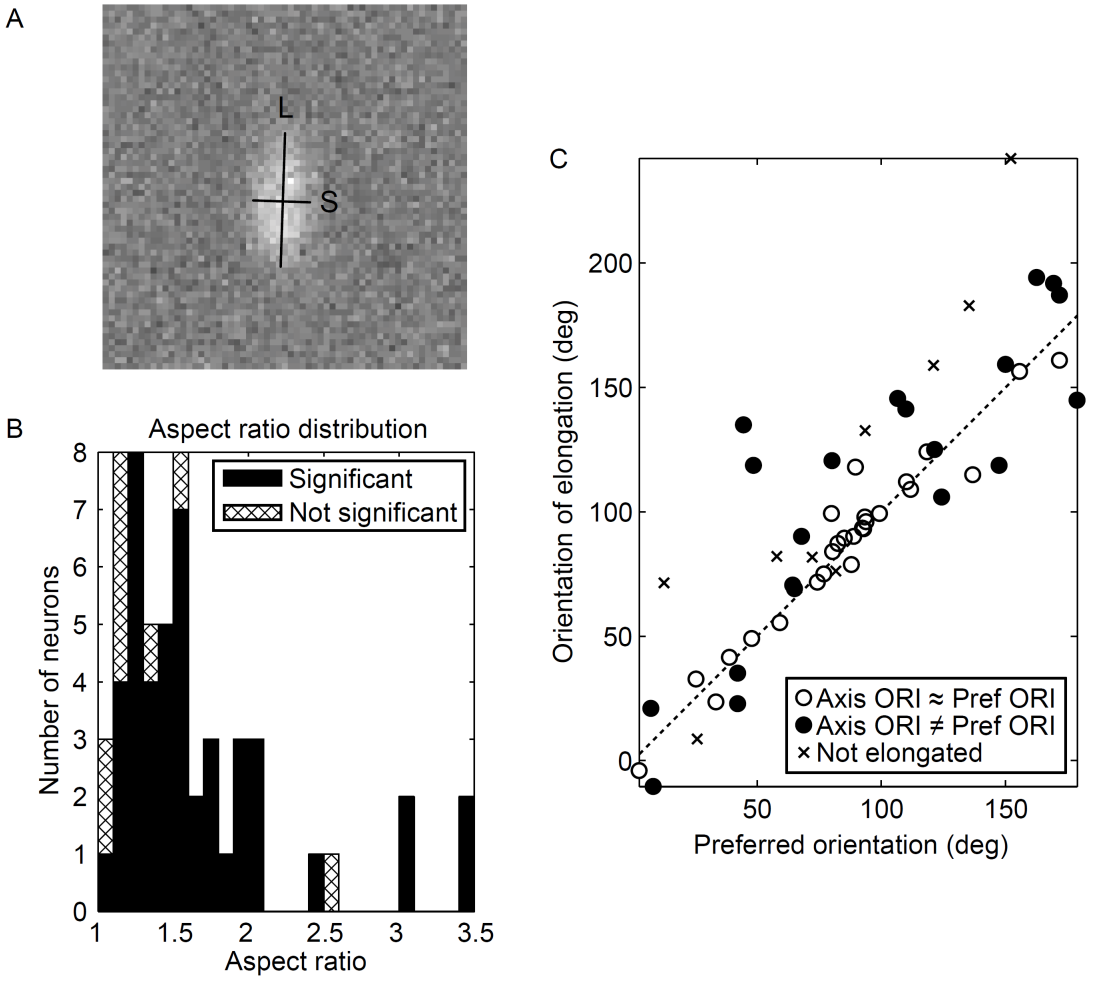

Figure 1.2: Spatial properties of a linear RF. A) An example of the linear RF spatial structure. L and S: long and short axes, respectively. This linear RF was an On-center type, as indicated by the white center. The aspect ratio (long axis/short axis) was 2.1. B) Distribution of aspect ratios. Filled and hatched bars indicate significantly (46) and not significantly (9) elongated RFs, respectively (N = 55, mean = 1.62 ± 0.57 SD, median = 1.44). C) Relationship between preferred orientations and the angles of the linear RF long axis. Filled and open circles indicate neurons whose preferred orientations were significantly and not significantly different to the corresponding long axis angles, respectively. Cross symbols indicate neurons whose RF centers were not significantly elongated.

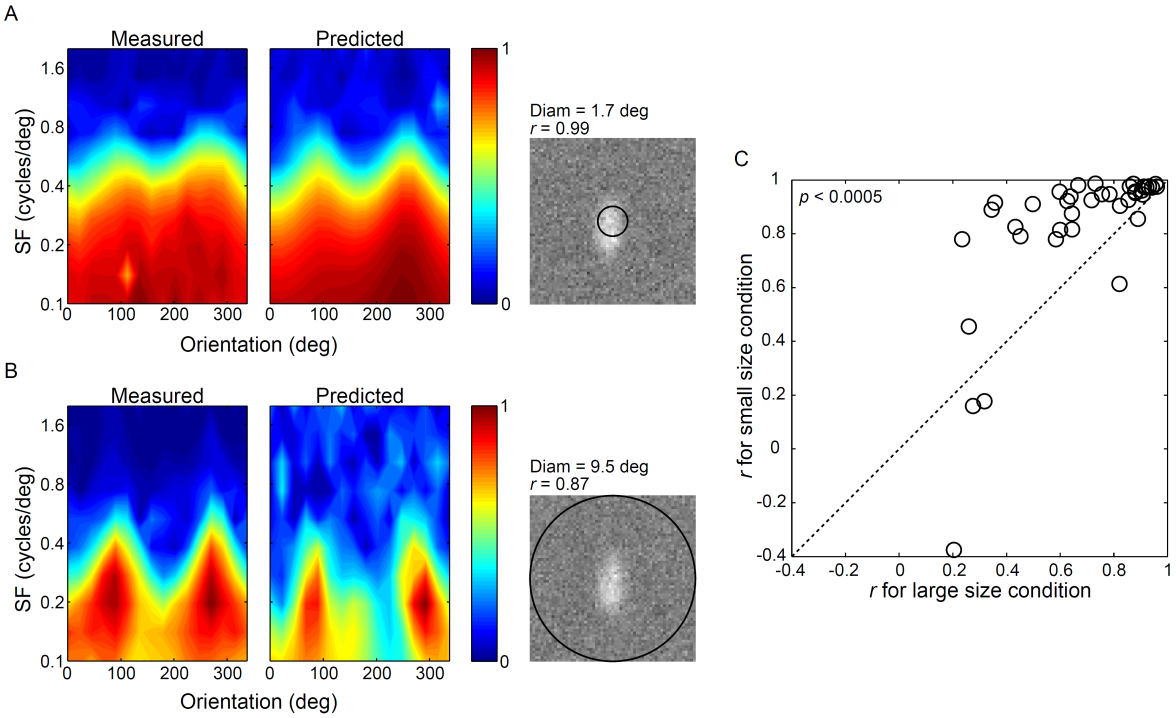

Figure 1.3: Comparison of measured and predicted tunings for small and large size conditions. A) SF×ORI tuning maps for the small size condition are depicted in the same manner as in Figure 1.1A (left, measured tuning map; right, predicted tuning map). In the rightmost panel, the open circle indicates the diameter and position of the drifting grating stimulus for a linear RF (stimulus diameter = 1.7 deg). For these data, the linear RF predicted well the measured responses to the grating stimuli (correlation coefficient, $r = 0.99$). B) SF×ORI tuning maps for the large size condition (stimulus diameter = 9.5 deg). In this case, the linear RF was a poor predictor ($r = 0.87$). Because we measured the RF structures twice just after each measurement of SF×ORI tuning maps for small and large size conditions, the inset RF structures in A and B look little bit different. C) Comparison of correlation coefficients (r) for small and large size conditions (N = 38).

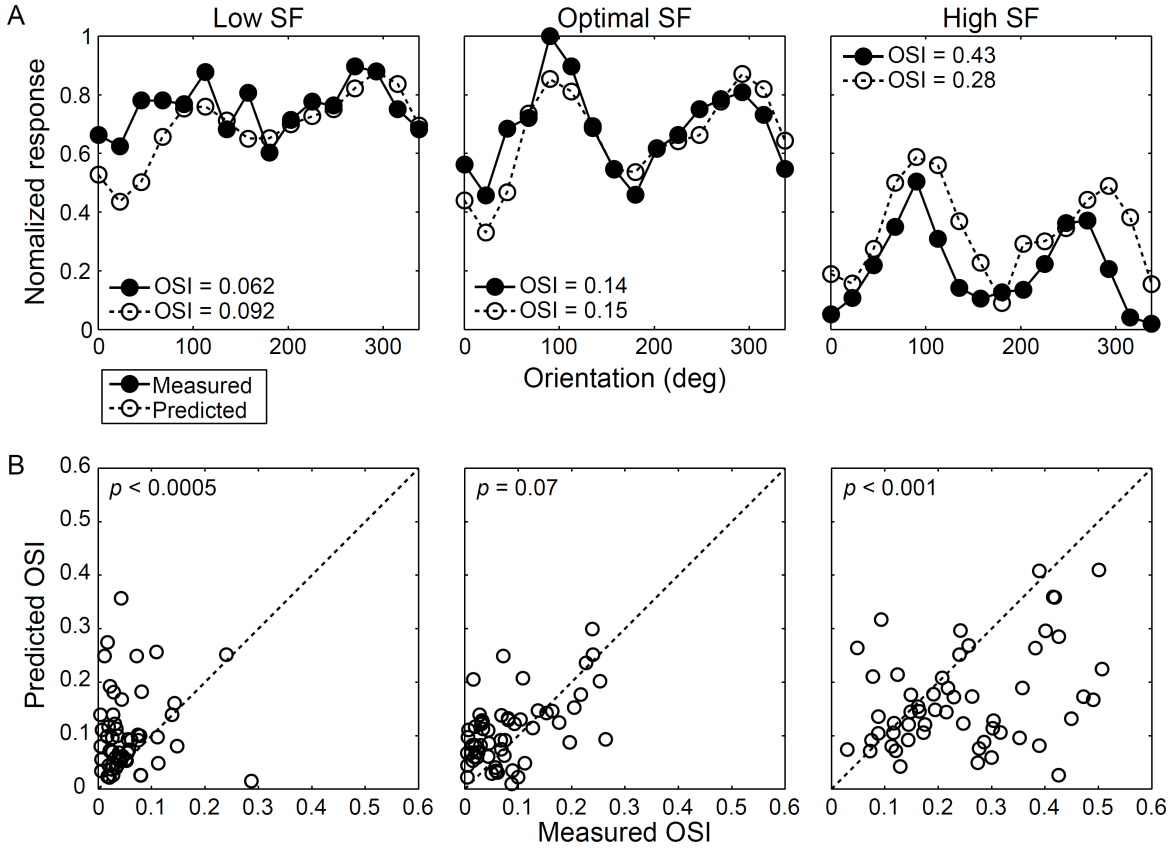

Figure 1.4: Comparison of measured and predicted orientation tunings. A) Orientation tuning curves at low, optimal and high SFs (left to right: low, optimal, high). Solid lines with filled circles and dashed lines with open circles indicate measured and predicted orientation tuning curves, respectively. B) Comparison of measured (X-axis) and predicted (Y-axis) OSIs (left to right: low, optimal, high) (N = 55). Predicted OSIs were significantly larger at the low SF, but smaller at the high SF than the measured ones. The mean predicted and mean measured OSI at low, optimal, and high SF are (0.10, 0.055), (0.11, 0.084), (0.17, 0.25), respectively.

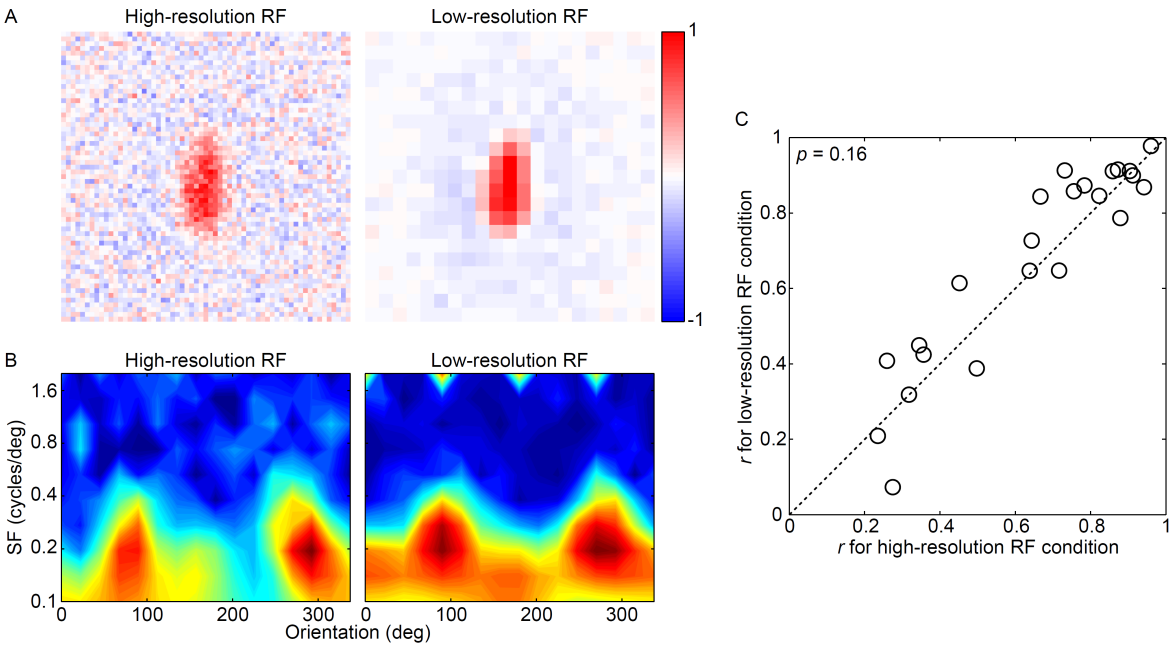

Figure 1.5: Comparison of two different resolution RFs and their SF×ORI tuning maps. A) Linear RF spatial structures reconstructed with two different resolution noise stimuli (left, high-resolution; right, low-resolution) depicted by a blue-white-red scale for lucidity (blue, off; red, on). The low-resolution RF has a bolder CRF surround than the high-resolution RF. B) SF×ORI tuning maps predicted from the resolution RFs in A (left, high-resolution; right, low-resolution). At SF = 0.1 to 0.2 cycles/deg and orientation = 0, 180 deg, the SF×ORI tuning map predicted by the low-resolution RF is depicted by a more reddish color, indicating the low-resolution RF lost sharp orientation tuning at low SFs. C) Comparison of prediction accuracies for the two resolution conditions (N = 23). Vertical and horizontal axes indicate the respective correlation coefficients. The prediction accuracy for the low-resolution RF was not significantly different from the high-resolution RF.

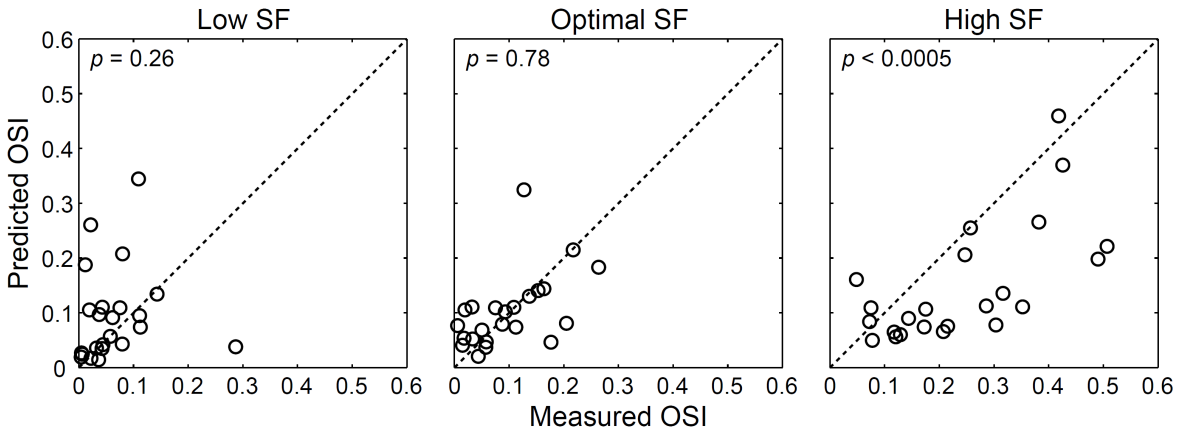

Figure 1.6: Comparison of measured OSIs with those predicted from low-resolution RFs (N = 23). While predicted OSIs were not significantly larger than those measured at the low SF, they were still significantly smaller than those measured at the high SF. The mean predicted and mean measured OSIs at low, optimal, and high SF were (0.094, 0.063), (0.10, 0.098), (0.15, 0.24), respectively.

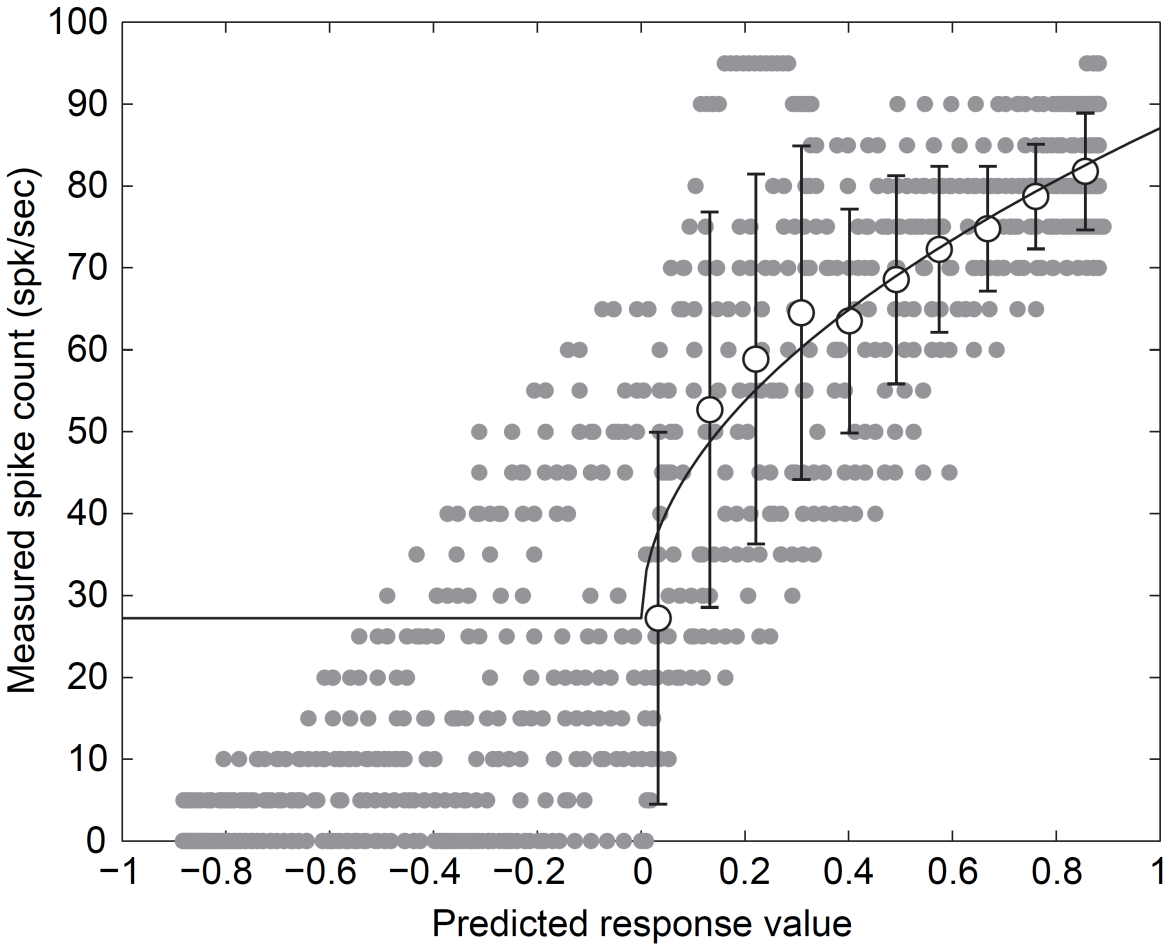

Figure 1.7: Non-linear relationship of a cell between measured spike counts and predicted response values for a particular SF and orientation condition. Gray filled circles indicate raw data; open circles indicate mean data in each bin. Error bars indicate 1 SD. We conducted these analyses with SF×ORI tuning data. Because predicted response values were normalized to the maximum predicted value for all parameters, predicted values in this panel distribute away from -1 and 1.

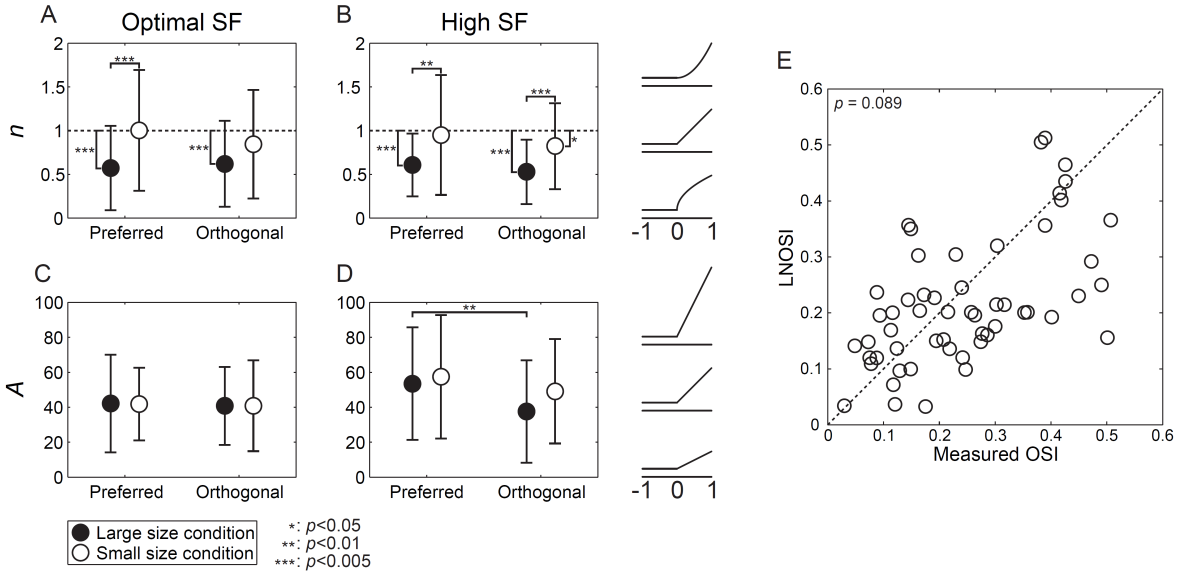

Figure 1.8: Non-linear response modulation functions. A–D) Comparisons of the non-linear response modulation functions. Filled and open circles indicate large and small stimulus size conditions, respectively. A), B) n from Equation 1.11 for the non-linear response modulation function at optimal and high SFs. C), D) A from Equation 1.11 for the non-linear response modulation function at optimal and high SFs. Error bars indicate 1 SD. Rightmost column illustrates the non-linear relationship curves in the manner depicted in Figure 1.7. The curve is linear when $n = 1$, convex (expansive) when $n > 1$, and convex (compressive) when $n < 1$. E) Comparison of measured OSIs with predicted OSIs acquired by using the non-linear response modulation functions (LNOSIs) at a high SF for large size grating stimuli (N = 55). LNOSIs were significantly greater than OSIs predicted from the linear RF. There was no significant difference between LNOSIs and measured OSIs.

References

Alitto, H. J., & Usrey, W. M. (2008). Origin and dynamics of extraclassical suppression in the lateral geniculate nucleus of the macaque monkey. *Neuron*, *57*, 135-146.

Allen, E. A., & Freeman, R. D. (2006). Dynamic spatial processing originates in early visual pathways. *J. Neurosci. 26*, 11763-11774.

Anzai, A., Ohzawa, I., & Freeman, R. D. (1999). Neural mechanisms for processing binocular information I. Simple cells. *J. Neurophysiol. 82*, 891-908.

Batschelet, E. (1981). *Circular statistics in biology (mathematics in biology)*. Academic Press Inc.

Bishop, P. O., Burke, W., & Davis, R. (1962). The identification of single units in central visual pathways. *J. Physiol. 162*, 409-431.

Bonin, V., Mante, V., & Carandini, M. (2005). The suppressive field of neurons in lateral geniculate nucleus. *J. Neurosci. 25*, 10844-10856.

Brainard, D. H. (1997). The Psychophysics Toolbox. *Spat. Vis. 10*, 433-436.

Carandini, M., & Ferster, D. (2000). Membrane potential and firing rate in cat primary visual cortex. *J. Neurosci. 20*, 470-484.

Chen, G., Dan, Y., & Li, C.-Y. (2005). Stimulation of non-classical receptive field enhances orientation selectivity in the cat. *J. Physiol. 564*, 233-43.

Chichilnisky, E. J. (2001). A simple white noise analysis of neuronal light responses. *Network (Bristol, England)*, *12*, 199-213.

Dan, Y., Atick, J. J., & Reid, R. C. (1996). Efficient coding of natural scenes in the lateral geniculate nucleus: experimental test of a computational theory. *J. Neurosci. 16*, 3351-3362.

DeAngelis, G. C., Ohzawa, I., & Freeman, R. D. (1993). Spatiotemporal organization of simple-cell receptive fields in the cat's striate cortex. I. General characteristics and postnatal development. *J. Neurophysiol. 69*, 1091-1117.

Duong, T., & Freeman, R. D. (2008). Contrast sensitivity is enhanced by expansive nonlinear processing in the lateral geniculate nucleus. *J. Neurophysiol. 99*, 367-372.

Enroth-Cugell, C., & Robson, J. G. (1966). The contrast sensitivity of retinal ganglion cells of the cat. *J. Physiol. 187*, 517-552.

Gardner, J. L., Anzai, A., Ohzawa, I., & Freeman, R. D. (1999). Linear and nonlinear contributions to orientation tuning of simple cells in the cat's striate cortex. *Visual Neurosci. 16*, 1115-1121.

Girman, S., & Lund, R. (2010). Orientation-specific modulation of rat retinal ganglion cell responses and its dependence on relative orientations of the center and surround gratings. *J. Neurophysiol. 104*, 2951-2962.

Henrie, J. A., & Shapley, R. M. (2001). The relatively small decline in orientation acuity as stimulus size decreases. *Vision Res. 41*, 1723-33.

Henry, G. H., Dreher, B., & Bishop, P. O. (1974). Orientation specificity of cells in cat striate cortex. *J. Neurophysiol. 37*, 1394-409.

Henry, G. H., Bishop, P. O., & Dreher, B. (1974). Orientation, axis and direction as stimulus parameters for striate cells. *Vision Res. 14*, 767-77.

Hochstein, S., & Shapley, R. M. (1976). Quantitative analysis of retinal ganglion cell classifications. *J. Physiol. 262*, 237-264.

Huang, L., Shou, T., Chen, X., Yu, H., Sun, C., & Liang, Z. (2006). Slab-like functional architecture of higher order cortical area 21a showing oblique effect of orientation preference in the cat. *NeuroImage, 32*, 1365-74.

Hubel, D. H., & Wiesel, T. N. (1959). Receptive fields of single neurones in the cat's striate cortex. *J. Physiol. 148*, 574-591.

Hubel, D. H., & Wiesel, T. N. (1962). Receptive fields, binocular interaction and functional architecture in the cat's visual cortex. *J. Physiol. 160*, 106-154.

Ikeda, H., & Wright, M. J. (1975). Spatial and temporal properties of 'sustained' and 'transient' neurones in area 17 of the cat. *Exp. Brain Res. 22*, 363-383.

Jones, H. E., Andolina, I. M., Oakely, N. M., Murphy, P. C., & Sillito, A. M. (2000). Spatial summation in lateral geniculate nucleus and visual cortex. *Exp. Brain Res. 135*, 279-284.

Leventhal, A. G., & Schall, J. D. (1983). Structural basis of orientation sensitivity of cat retinal ganglion cells. *J. Comp. Neurol. 220*, 465-475.

Levick, W. R., & Thibos, L. N. (1980). Orientation bias of cat retinal ganglion cells. *Nature*, *286*, 389-390.

Li, B., Peterson, M. R., & Freeman, R. D. (2003). Oblique effect: a neural basis in the visual cortex. *J. Neurophysiol. 90*, 204-17.

Movshon, J. A., Thompson, I. D., & Tolhurst, D. J. (1978). Spatial and temporal contrast sensitivity of neurones in areas 17 and 18 of the cat's visual cortex. *J. Physiol. 283*, 101-120.

Naito, T., Osaki, H., Sadakane, O., Okamoto, M., Shimegi, S., & Sato, H. (2009). Neural mechanisms of orientation selectivity in cat lateral geniculate nucleus. *The XXXVI International Congress of Physiological Sciences (IUPS2009)*.

Naito, T., Sadakane, O., Okamoto, M., & Sato, H. (2007). Orientation tuning of surround suppression in lateral geniculate nucleus and primary visual cortex of cat. *Neuroscience*, *149*, 962-975.

Nolt, M. J., Kumbhani, R. D., & Palmer, L. a. (2007). Suppression at high spatial frequencies in the lateral geniculate nucleus of the cat. *J. Neurophysiol. 98*, 1167-1180.

Okamoto, M., Naito, T., Sadakane, O., Osaki, H., & Sato, H. (2009). Surround suppression sharpens orientation tuning in the cat primary visual cortex. *Eur. J. Neurosci. 29*, 1035-1046.

Ozeki, H., Finn, I. M., Schaffer, E. S., Miller, K. D., & Ferster, D. (2009). Inhibitory stabilization of the cortical network underlies visual surround suppression. *Neuron*, *62*, 578-592.

Pelli, D. G. (1997). The VideoToolbox software for visual psychophysics: transforming numbers into movies. *Spat. Vis. 10*, 437-442.

Shen, W., Liang, Z., & Shou, T. (2008). Weakened feedback abolishes neural oblique effect evoked by pseudo-natural visual stimuli in area 17 of the cat. *Neurosci. Lett. 437*, 65-70.

Shou, Tiande, & Leventhal, A. G. (1989). Organized arrangement of orientation-sensitive relay cells in the cat's dorsal lateral geniculate nucleus. *J. Neurosci. 9*, 4287-4302.

Shou, Tiande, Leventhal, A. G., Thompson, K. G., & Zhou, Y. (1995). Direction biases of X and Y type retinal ganglion cells in the cat. *J. Neurophysiol. 73*, 1414-1421.

Sillito, A. M., Cudeiro, J., & Murphy, P. C. (1993). Orientation sensitive elements in the corticofugal influence on centre-surround interactions in the dorsal lateral geniculate nucleus. *Exp.l Brain Res. 93*, 6-16.

Smith, E. L., Chino, Y. M., Ridder, W. H., Kitagawa, K., & Langston, A. (1990). Orientation bias of neurons in the lateral geniculate nucleus of macaque monkeys. *Visual Neurosci. 5*, 525-545.

Solomon, S. G., Tailby, C., Cheong, S.-K., & Camp, A. J. (2010). Linear and nonlinear contributions to the visual sensitivity of neurons in primate lateral geniculate nucleus. *J. Neurophysiol. 104*, 1884-1898.

Sompolinsky, H., & Shapley, R. (1997). New perspectives on the mechanisms for orientation selectivity. *Curr. Opin. Neurobiol. 7*, 514-522.

Soodak, R. E., Shapley, R. M., & Kaplan, E. (1987). Linear mechanism of orientation tuning in the retina and lateral geniculate nucleus of the cat. *J. Neurophysiol. 58*, 267-275.

Sun, C., Chen, X., Huang, L., & Shou, T. (2004). Orientation bias of the extraclassical receptive field of the relay cells in the cat's dorsal lateral geniculate nucleus. *Neuroscience*, *125*, 495-505.

Tavazoie, S. F., & Reid, R. C. (2000). Diverse receptive fields in the lateral geniculate nucleus during thalamocortical development. *Nat. Neurosci. 3*, 608-616.

Usrey, W. M., Alonso, J.-M., & Reid, R. C. (2000). Synaptic interactions between thalamic inputs to simple cells in cat visual cortex. *J. Neurosci. 20*, 5461-5467.

Vidyasagar, T. R., & Urbas, J. V. (1982). Orientation sensitivity of cat LGN neurones with and without inputs from visual cortical areas 17 and 18. *Exp. Brain Res. 46*, 157-169.

Volgushev, M., Pernberg, J., & Eysel, U. T. (2000). Comparison of the selectivity of postsynaptic potentials and spike responses in cat visual cortex. *Eur. J. Neurosci. 12*, 257-263.

Zar, J. H. (1996). *Biostatistical Analysis*. Prentice Hall College Div.

Theme 2

Spatiotemporal receptive field structures in retinogeniculate connections of cat

Abstract

The spatial structure of the receptive field (RF) of cat lateral geniculate nucleus (LGN) neurons is significantly elliptical, which may provide a basis for the orientation tuning of LGN neurons, especially at high spatial frequency stimuli. However, the input mechanisms generating this elliptical RF structure are poorly defined. I therefore compared the spatiotemporal RF structures of pairs of retinal ganglion cells (RGCs) and LGN neurons that form monosynaptic connections based on the cross-correlation analysis of their firing activities.

I found that the spatial RF structure of both RGCs and LGN neurons were comparably elliptical and oriented in a direction toward the *area centralis*. Additionally, the spatial RF structures of pairs with the same response sign were often overlapped and similarly oriented. I also found there was a small population of pairs with RF structures that had the opposite response sign and were spatially displaced and independently oriented. Finally, the temporal RF structure of a RGC was tightly correlated with that of its target LGN neuron, though the response duration of the LGN neuron was significantly longer.

My results suggest that the elliptical RF structure of a LGN neuron is mainly inherited from the primary projecting RGC and is affected by convergent inputs from multiple RGCs. I discuss how the convergent inputs may enhance the stimulus feature sensitivity of LGN neurons.

Introduction

In the early visual system of mammals, visual information is received by the retina and then relayed to the primary visual cortex (V1) via the lateral geniculate nucleus (LGN) (Hubel and Wiesel, 1962, 1977). Through these stages, receptive field (RF) properties, such as orientation, spatial frequency (SF), and temporal frequency (TF) tuning, are successively elaborated, which expands the sensitivity for various visual features in neurons of the early visual system (Hubel and Wiesel, 1959, 1962; Enroth-Cugell and Robson, 1966; Campbell et al., 1969; Movshon et al., 1978; Derrington and Fuchs, 1979; Frishman et al., 1987).

In the LGN, it had been commonly believed that neurons exhibit only weak or no orientation selectivity, and their RFs are almost circular (Hubel and Wiesel, 1959, 1962). However, more recent studies have reported that LGN neurons exhibit moderate orientation sensitivity in cat (Soodak et al., 1987; Shou and Leventhal, 1989; Smith et al., 1990; Suematsu et al., 2012; Naito et al., 2013), mouse (Scholl et al., 2013; Zhao et al., 2013; Niell, 2013), and marmoset (Cheong et al., 2013) due to an elliptical RF structure (Soodak et al., 1987; Ahmed and Hammond, 1991; Suematsu et al., 2012).

There are at least two possible explanations for how the elliptically elongated RF structure of LGN neurons is generated. One is that the spatial RF structure of a retinal ganglion cell (RGC), which is an input source for LGN neurons, is also elongated such that the target LGN neuron directly reflects this structure. Rodieck and Stone (1965) and Hammond (1974), for example, reported the ellipticity of the spatial RF structure of cat RGCs. In addition, it is commonly thought that the connection between an RGC and LGN neuron is essentially one-to-one, because both the projecting RGC afferent and target LGN neuron have very similar spatial RF structures and properties (Soodak et al., 1987; Smith et al., 1990). The other explanation is that a single LGN neuron receives convergent inputs from multiple

RGCs sharing in-line RF positions that elongate the RF of the LGN neuron (Tavazoie and Reid, 2000). Several studies have shown the possibility of convergent inputs in retinogeniculate connections (Usrey et al., 1999; Moore et al., 2011), which are important for creating a diversity of RF structures in different LGN neurons (Alonso et al., 2006). However it is still unclear how convergent projections in retinogeniculate connections contribute to the spatial and temporal RF structure of LGN neurons.

To clarify the underlying mechanism involved, I simultaneously recorded the single-unit activities of RGCs and LGN neurons of cat during the presentation of two-dimensional dynamic dense noise stimuli and analyzed their RF structures, which were reconstructed by the reverse correlation technique using electrophysiologically-identified retinogeniculate connections. I found that RGCs and LGN neurons exhibited elliptical spatial RF structures, and that an RGC projection of the same response sign was the primary contributor to the generation of the RF center of the LGN neuron, while an RGC projection of the opposite response sign was responsible for enhancing the antagonistic surround. In addition, the temporal RF structure of an RGC was tightly correlated with its target LGN neuron, although the response duration was significantly shorter. These results suggest that the elongated RF of LGN neurons is mainly inherited from that of the primary-projecting RGC and that convergent inputs from multiple RGCs improve the stimulus feature sensitivity of LGN neurons, presumably by contributing to more efficient processing in the visual cortex.

Methods

All experimental protocols were approved by the Research Ethics Committee of Osaka University. All animal procedures were performed in accordance with the National Institute of Health Guidelines for the Care and Use of Laboratory Animals and the Guidelines of the Animal Care Committee of the Osaka University Medical School. All efforts were made to reduce the number of animals used.

Preparation

Four adult cats weighing 3.1–4.1 kg were used. Initially, atropine (0.1 mg, i.m.) was injected as premedication. Animals were anesthetized with ketamine hydrochloride (Ketalar; Sankyo, Tokyo, Japan; 25 mg/kg), placed in a stereotaxic head holder, and then anesthetized with a mixture of N_2O/O_2 (1:1) after tracheal intubation. A catheter was placed in the femoral vein. During the entire experimental period (–48 hrs), to paralyze and maintain animals under artificial ventilation and to minimize eye movements, a mixture of N_2O/O_2 (1:1) was continuously supplied, and a solution of sodium pentobarbital (Somnopentyl; Kyoritsu, Tokyo, Japan; 1 mg/kg/h, i.v.) in Ringer's solution for anesthesia and a mixed solution of pancuronium bromide (Mioblock; MSD, Tokyo, Japan; 0.1 mg/kg/h, i.v.) and glucose in Ringer's solution for paralysis were continuously infused through the femoral vein at 0.5 and 1.5 ml/kg/h, respectively. An electroencephalogram (EEG), electrocardiogram, and heart rate were continuously monitored throughout the experiments.

A local anesthetic, lidocaine (Xylocaine; AstraZeneca, Osaka, Japan), was administered at pressure points and around surgical incisions. The depth of anesthesia was judged to be adequate because no significant heart rate change (>10%) was observed when the incision was made. The nictitating membrane was retracted and the pupil was dilated with topical application of tropicamide

(0.5%), atropine (1%), and phenylephrine hydrochloride (0.5%) (Mydrin-P; Santen, Osaka, Japan). The eyes were refracted using contact lenses in order to focus them onto a cathode-ray tube (CRT) monitor. Body temperature was maintained at 38 °C with a thermostatically controlled heating pad. The end-tidal CO_2 concentration was adjusted to 4–5%.

Surgical procedures are described in detail elsewhere. A scalp was dissected after injecting lidocaine over the skull. For chiasmic stimulations, two openings were made in the skull, dura, and arachnoid near each side of the sagittal suture above and a pair of stimulation electrodes was inserted near each side of the optic chiasma (14.5 mm AP, 2.0 mm ML; Stone and Fukuda, 1974; Fukuda and Stone, 1974). After the recordings of an RGC, I stimulated the optic chiasma by passing a current (monophasic, a rectangular pulse of 50 μs, 0.5–2 mA; Mihashi et al., 2011) and measured the response latency of the RGC for identification of the cell type (X, Y, or W) (see "Off-line Data Analysis" section).

For retinal recordings, a sclera was carefully stitched with a nylon suture to a fixation ring mounted on the stereotaxic head-holder. An opening was made in the sclera through which an intraocular guide tube was inserted and a tungsten electrode (FHC, USA; 3–5 MΩ) was inserted intraocularly through the guide tube (Takao et al., 2000, 2002). I carried the electrode forward while watching the fundus oculi with a funduscope and judged when the electrode contacted the retina by both the fundus image and the audio-monitoring of the spiking activity. For geniculate recordings, an opening was made in the skull, dura, and arachnoid above the LGN through which a tungsten electrode was vertically inserted (Naito et al., 2007; Suematsu et al., 2012).

Visual Stimulation, Recordings, and On-line Data Analysis

Extracellular recordings were made from RGCs and LGN neurons using the tungsten electrodes.

All stimuli were generated using custom-made MATLAB (Mathworks, USA) programs with Psychtoolbox (Brainard, 1997; Pelli, 1997) and presented on a gamma-corrected CRT monitor (FlexScan FX-E7, EIZO; mean luminance, 70 cd/m^2; screen size, 40 × 30 cm^2) placed 57 cm in front of the cat using two different settings (resolution 1280 × 960 pixels, refresh rate 85 Hz; or 1600 × 1200 pixels at 75 Hz). Electrophysiological signals were amplified using an AC amplifier (AM-1800; A-M Systems, USA) and sent to a slicer (Nihon Kohden, Tokyo, Japan), which performed on-line threshold-based spike detection. Digital pulses obtained from the slicer were acquired using an IO board (AIO-160802L-LPE, CONTEC, Osaka, Japan) and sampling rate of 20 kHz. Peristimulus time histograms (PSTHs) of the unit responses were constructed and analyzed off-line. I acquired the amplified raw signals for off-line spike sorting (see "Off-line Data Analysis" section) and EEG signals to monitor an animal's vital conditions.

The center position of the RF was first assessed by carefully varying the spatial location of a small uniform patch stimulus. I then presented two-dimensional dynamic dense noise stimuli (size, 9.6 × 9.6 or 16 × 16 deg divided into 31 × 31 or 61 × 61 grids; duration = 10 minutes) every two frames of the monitor refresh at the assessed position on the CRT monitor (median spike rates of RGCs and LGN neurons = 97 and 78 spk/s, respectively), and the spatiotemporal RF structure was reconstructed using the reverse correlation technique (Jones and Palmer, 1987).

Off-line Data Analysis

To conduct off-line spike sorting, I used Wave_Clus (Quiroga et al., 2004) running on MATLAB. Raw data were band-pass filtered, spikes were detected from the filtered data on the basis of a particular threshold (usually threefold baseline noise level calculated from absolute values of the filtered data), features of the detected spikes were extracted with the wavelet analysis, and the detected spikes were clustered into multiple single units on the basis of the extracted features. I confirmed the

existence of 3-ms or more refractory period in the auto-correlogram of spike trains for all neurons.

RGCs were classified as X-, Y-, or W-cells based on the second and first harmonic (F2/F1) ratio of the response, response latency, and RF size (Enroth-Cugell and Robson, 1966; Stone and Fukuda, 1974; Hochstein and Shapley, 1976), while LGN neurons were classified as X- or Y-cells based on the F2/F1 ratio only (Bonin et al., 2005). A spatiotemporal RF structure was reconstructed from single-unit activity (typically 3000–25000 spikes) and the reverse correlation technique. I fitted the reconstructed spatial RF structures at the peak response latency with the two-dimensional difference of Gaussians (2DDoG) model, as previously described (Suematsu et al., 2012). This approach provided the center position, aspect ratio, elongation angle (angle between the long axis of the RF and horizontal meridian, solid arc in Figure 2.1A), and size (2SD of the fitted center Gaussian) of the spatial RF structures. In addition, I calculated the eccentric angle, angle between the horizontal meridian and the line connecting the RF center position with the *area centralis* (dotted arc in Figure 2.1A). Elongation angles and eccentric angles essentially ran from -180 to 180 deg. I chose elongation angles from cells so that the difference in eccentric and elongation angles became acute. Note that the population of eccentric angle data distributed in the range between 0 and 180 deg, especially for RGCs (RGC, N for eccentric angle < 0 and ≥ 0 were 15 and 153, respectively; LGN neurons, N = 40 and 49, respectively). This is because the number of recoded RGCs was larger at the ventral side of the *area centralis* than that at the dorsal side.

The cross-correlogram (XC) was calculated from the single-unit activity elicited by noise stimuli using the following equation (Usrey et al., 1999) to assess monosynaptic retinogeniculate connections:

$$XC(\tau) = \Sigma_t R_i(t) R_j(t+\tau) \qquad (2.1)$$

, where $R_i(t)$ indicates the response (spikes/sec) of the i-th single unit at the t-th time bin (width = 0.1 ms). Indices i and j indicate retinal and geniculate single units, respectively. I filtered the raw XC with a band-pass filter whose frequency characteristic was Gaussian shaped with mean = 1 kHz and variance = 707 Hz. These values were determined to make the frequency properties analogous to the filter used in a previous study (Usrey et al., 1999). To estimate the baseline noise level, I calculated the mean and SD of the filtered XC between ± 10 ms after removing the 2-5 ms interval. I defined a significant retinogeniculate connection when the filtered XC in the 2-5 ms interval exceeded the baseline + 5 SD. Also I calculated the efficacy (peak XC amplitude normalized by the number of retinal spikes) and contribution (peak XC amplitude normalized by the number of geniculate spikes) as the measure of the connection strength (Usrey et al., 1999)

To quantitatively evaluate a spatial relationship between structures, including distance between the RF center positions, and each RF size, the overlap ratio was calculated from the spatial RF structures of a retinogeniculate pair that had monosynaptic connections using the following equation:

$$\text{overlap ratio} = (S_i+S_j)/D \quad (2.2)$$

, where S and D indicate the RF size and the distance between the RF center positions of an RGC and its connected LGN neuron, respectively. More specifically, S was defined as the distance from the RF center position to the intersection with an ellipse approximating the RF (2 SD of the center Gaussian) along line D (see Figure 2.5C, inset). Overlap ratios greater than 1 indicate that center regions of the spatial RF structures of the connected pair are overlapped, while those less than 1 indicate they are not. This measure contains the inter-RF-center distance and RF sizes of the RGC and LGN neuron, and thus

is assumed as the distance normalized by the RF sizes.

Singular value decomposition (SVD) of the spatiotemporal RF structure was performed to extract the temporal RF structure. SVD allows me to decompose a spatiotemporal RF structure into three components: a spatial RF structure, a temporal RF structure (two eigenvector matrices), and an amplitude (an eigenvalue matrix) (Wolfe and Palmer, 1998). In practice, to conduct SVD, I used the MATLAB command `svd` after reshaping a 3D spatiotemporal RF structure (space × space × time) into 2D (space × time). The separability of spatial and temporal RF structures was confirmed by the calculating the percentage of total power captured by the first eigenvalue. For my data, this measure ran between 20% and 72% for the RGCs and between 8 and 54% for the LGN neurons, whose ranges were somewhat lower than a previous study (Wolfe and Palmer, 1998, 36%–90%). This difference was probably caused by the resolution of the RF structures; I used two-dimensional noise stimuli which have total 961 (= 31 × 31) or 3721 (= 61 × 61) positions, whereas they used one-dimensional 16-position bar stimuli. To compare the temporal RF structure between each retinogeniculate pair, I first normalized the intensities by the first response peak value and then extracted the peak latency of the first response (primary peak latency, P1), the peak latency of the rebound response (secondary peak latency, P2), the duration of the first response (full width at half maximum, FWHM1), the duration of the rebound response (full width at half minimum, FWHM2), and the relative amplitude of the rebound response to first response (minimum intensity, m) (Figure 2.8A).

Histology of the LGN

At the end of each penetration for the LGN recordings, at least three electrolytic lesions were made along the track by passing a current (DC, 3–4 μA, 10 sec, tip negative). Lesions were separated by intervals of more than 300 μm. After the recording experiments, the animals were deeply anesthetized

with sodium pentobarbital (60 mg/kg, i.v.) and perfused transcardially with phosphate buffered saline (PBS, pH 7.4). Blocks of the dorsolateral thalamus were obtained and immersed in 30% sucrose in 4% paraformaldehyde for 36–48 h. Frozen sagittal sections 80-μm thick were sliced on a microtome and kept in PBS. Sections were stained for cytochrome oxidase or Nissl substance. The laminar locations of the recording sites were then identified under a light microscope. Shrinkage in the geniculate tissues was corrected for by multiplying the ratio of the measured lesion distance by the value calculated from the micrometer reading. LGN layers were classified as layers A, A1 or C.

Results

I obtained the single-unit activities of 168 RGCs (X, Y, W = 136, 31, 1) and 34 LGN neurons (Layer A, A1, C = 9, 4, 11; X, Y, unknown = 12, 1, 21). For all 26 retinogeniculate pairs monosynapticaly connected, as confirmed by the XC, cell types and their combinations are summarized in Table 2.1. RF positions of the RGCs were not confined to a particular retinal location (from nasal 30 deg to temporal 14 deg, from ventral 33 deg to dorsal 13 deg). Among the 105 retinogeniculate pairs analyzed, 26 pairs exhibited significant retinogeniculate connections according to cross-correlation analysis. I compared the spatiotemporal RF structures of the RGCs (N = 168) and the LGN neurons (N = 89; 34 neurons recorded in the current study and 55 neurons recorded in my previous study, Suematsu et al., 2012).

Table 2.1: Cell types for the retinogeniculate pairs.

		LGN neuron			
		X	Y	Unknown	
RGC	X	7	3	11	21
	Y	2	0	3	5
	W	0	0	0	0
		9	3	14	26

Comparison of Spatial RF Structures of RGCs and LGN neurons

Figure 2.1A shows a representative example of the spatial RF structure of an X-type RGC at the peak response latency (40 ms). The spatial RF structure was elliptically elongated ON-center and OFF-surround. For most pairs, the surround structures were so obscure that I did not analyze them parametrically. The aspect ratio, elongation angle, and eccentric angle were 1.38, 142 deg, and 123 deg,

respectively. Overall, I focused on these three parameters for my analysis of all RGCs and LGN neurons and their comparisons.

Figure 2.1B shows the distributions of the aspect ratio of the spatial RF structures. Black and gray bars indicate RGCs (N = 168, mean = 1.56, median = 1.38) and LGN neurons (N = 89, mean = 1.62, median = 1.44), respectively. The aspect ratio of the spatial RF structure of the RGCs was not significantly different from that of the LGN neurons (two-sample Kolmogorov–Smirnov test, $p = 0.64$), indicating that the RGCs had RFs as elongated as those of the LGN neurons.

Figure 2.1C shows a relationship between the elongation angles and eccentric angles. Black and gray circles indicate RGCs and LGN neurons, respectively. For both RGCs and LGN neurons, most data points were distributed around the diagonal line (dotted line). The regression lines calculated with the least-squares method are Y=1.2X-15 (coefficient of determination, $R^2 = 0.72$) for the RGCs (solid line) and Y=1.1X-7.0 ($R^2 = 0.80$) for the LGN neurons (gray solid line). These results suggest that the RF structure of both the RGCs and LGN neurons were elongated in a direction toward the *area centralis*. To verify this possibility in detail, I calculated differences between the elongation angles and the eccentric angles (Figure 2.1D). For both the RGCs and the LGN neurons, the distributions were significantly different from a uniform distribution and were biased to 0 deg (RGC, SD = 48 deg, v-test, $p = 0.015$; LGN neuron, SD = 45 deg, $p = 0.0025$), further suggesting that the spatial RF structures of both the RGCs and the LGN neurons tended to be oriented in a direction toward the *area centralis*. There was no significant difference between the two distributions (two-sample Kolmogorov–Smirnov test, $p = 0.70$).

These results support the possibility that the elongated RF structure of a LGN neuron is derived from that of its input-source RGC. To assess this possibility directly, I compared the spatial RF structures

of pairs with retinogeniculate connections.

Relationship of Spatial RF Structures of Connected pairs

I identified 26 pairs of single units with electrophysiologically assessed (see Methods, Equation 2.1) retinogeniculate connections from simultaneously recorded RGCs and LGN neurons (Figure 2.2). I found that there were two types of retinogeniculate connections between an RGC-LGN neuron pair: those that exhibited RFs with the same response sign (20/26) and those that exhibited RFs with the opposite response sign (6/26). Figures 2.3 and 2.4 show typical examples of same- and opposite-response-sign pairs, respectively.

Figure 2.3A shows an example of an XC (see Methods, Equation 2.1) with a peak at 3.8 ms, indicating that there was a monosynaptic connection between the RGC and the LGN neuron. Figure 2.3B shows the spatiotemporal RF structures of this pair (top, RGC; bottom, LGN neuron). The RGC exhibited a horizontally-elongated OFF-center RF structure (aspect ratio and elongation angle = 1.95 and -3 deg, respectively), which is similar to that of the target LGN neuron (aspect ratio and elongation angle = 1.65 and 0 deg, respectively) and precedes it by about 10 ms. Note that although there were large separations between 3.8 ms from the XC and 10 ms from the RFs, I attribute this to stimuli being refreshed at 75 or 85 Hz (see Methods; one-frame duration = 13 or 12 ms). The overlaid RF structures at each peak response latency (RGC, 44 ms; LGN neuron, 55 ms) shown in Figure 2.3C (Pearson product-moment correlation coefficient, $r = 0.60$, t-test of a correlation coefficient, $p = 8.7\times10^{-97}$) further suggests that the elongated RF structure of LGN neurons directly reflects that of their projecting RGCs.

There was a small population of retinogeniculate pairs with monosynaptic connections that had opposite signs for the RF center. Figure 2.4A shows an example of an XC with a peak at 3.6 ms,

indicating a monosynaptic connection between the RGC and the LGN neuron. Figure 2.4B shows the spatiotemporal RF structures of the pair (top, RGC; bottom, LGN neuron). This RGC exhibited a horizontally-elongated OFF-center RF structure (aspect ratio and elongation angle = 1.44 and 174 deg, respectively), while the target LGN neuron exhibited an ON-center RF structure (aspect ratio and elongation angle = 1.18 and 180 deg, respectively). Figure 2.4C shows overlaid images of the RFs shown in Figure 2.3B at each peak response latency (RGC, 47 ms; LGN neuron, 57 ms). These two spatial RF centers were not overlapped, rather the OFF-center RGC seemed to partially overlap the OFF-surround region of the LGN neuron (r = 0.18, t-test of a correlation coefficient, $p = 5.7\times10^{-27}$), suggesting that this RGC contributed to generating the antagonistic surround region of the target LGN neuron.

These above results suggest that there are two types of retinogeniculate connections; one with the same response sign, which probably generates the RF center of the LGN neuron, and the other with the opposite response sign which, may correspond to the RF surround. To examine this hypothesis in detail, I compared the RF properties (difference of elongation angles, distance between RF center positions, overlap ratio, and r between spatial RF structures) between each retinogeniculate pair.

Comparison between Same- and Opposite-Response-Sign Pairs

Figure 2.5A shows the distribution of the difference of elongation angles between the spatial RF structures of connected pairs. A majority of pairs with the same response sign (17/20, black bars) were distributed within a difference of 0–20 deg, while data for pairs with the opposite response sign were more evenly distributed (N = 6, gray bars). There was a significant difference between the medians of these two distributions (5.2 and 50.4 deg, respectively; Wilcoxon rank sum test, p = 0.019; bootstrap test based on Wilcoxon rank sum test statistic, n = 10000, p = 0.0028). These results indicate that the

same-response-sign pairs exhibited similar oriented RF structures, while the opposite-response-sign pairs did not.

Figure 2.5B shows the distributions of the distances between the RF center positions of the pairs. For the same-response-sign pairs (left, black dots), data points were distributed widely, ranging from 0.16 to 1.43 deg (mean and median = 0.86 and 1.05 deg, respectively). On the other hand, the opposite-response-sign pairs (right, gray dots) tended to exhibit relatively longer distances, ranging from 0.84 to 1.56 deg (mean and median = 1.25 and 1.27 deg, respectively, Wilcoxon rank sum test, $p = 0.09$), suggesting that for these pairs, the RF center region of the RGCs overlapped with the RF surround region of the target LGN neurons.

Because, however, the RF sizes are different from each other, I calculated the overlap ratio as the distance normalized by the RF sizes of the pairs. Figure 2.5C shows the distributions of the overlap ratios (see Methods, Equation 2.2) between the RF center regions of all pairs. Half of the same- (10/20) and opposite- (3/6) response-sign pairs had overlap ratios greater than 1, indicating their RFs overlapped each other's center region, whereas the other half had overlap ratios smaller than 1, indicating those RFs did not overlap. The same-response-sign pairs exhibited a wide range of overlap ratios (0.53–12, geometric mean = 1.9), while the opposite-response-sign pairs had a significantly smaller range (0.44–2.6, geometric mean = 1.0; t-test after logarithmic transformation, $p = 0.046$). This result indicates that the RGCs in the same-response-sign pairs tended to exhibit spatial RF structures that overlap the LGN neurons' RF center and surround regions, whereas those in the opposite-response-sign pairs exhibited RFs overlapping only the surround region of the RFs of the LGN neurons.

Figure 2.5D shows the distributions of r between the spatial RF structures of different pairs.

Most data are distributed on the positive side of the abscissa, indicating that the RF regions, be they center or surround, can overlap if their response signs are the same. In other words, ON-center RGCs overlap the ON-center region of ON-center LGN neurons (same-response-sign pairs) or the ON-surround region of OFF-center LGN neurons (opposite-response-sign pairs) and vice versa.

It could be argued that in the same-response-sign pairs of Figure 2.5B there exist two clusters (left, black dots), one with relatively small differences in the RF center positions (SHORT, distance < 0.8 deg, N = 9), in which the RFs of the pairs can overlap each other's center region, and one with relatively large differences (LONG, distance ≥ 0.8 deg, N = 11), in which the RF center region of the RGCs probably overlap the RF surround region of the target LGN neurons rather than the center. I compared other spatial RF properties (difference of elongation angles, overlap ratio, and r) between these two groups, finding significant differences in the overlap ratio and r (overlap ratio, geometric mean for SHORT and LONG = 5.2 and 0.80, respectively, median = 5.3 and 0.82, respectively, Wilcoxon rank sum test, $p = 2.0\times10^{-4}$; r, mean = 0.56 and 0.098, respectively, median = 0.59 and 0.034, respectively, Wilcoxon rank sum test, $p = 6.3\times10^{-4}$), but not in the elongation angles (mean for SHORT and LONG = 12 and 13, respectively, median = 3 and 13, respectively, Wilcoxon rank sum test, $p = 0.25$). These results are as expected, since the longer distance makes a smaller overlap ratio (see Equation 2.2) and the LONG pairs have RFs with the same response sign at their center positions. Thus, the two clusters show differences just in their RF center distances, and any functional differences, such as displaced inputs being orientation-independent, are not suggested. However, because the number of connected pairs is small, future studies are necessary to validate these conclusions.

Taken together, it is suggested that a single LGN neuron receives two types of convergent inputs from RGCs, one which exhibits the same response sign and a similarly oriented RF to primarily

determine the RF center of the target LGN neuron, and another which exhibits the opposite response sign and an independently oriented RF to primarily determine the antagonistic RF surround (Figure 2.5E).

Next, I compared connection strength between same- and opposite-response-sign pairs. To this aim, I compared the efficacies and contributions (see Methods) between the same- and opposite-response-sign pairs (Figures 2.6A, F). I also investigated the relationships between the efficacies/contributions and the RF properties of the pairs (Figures 2.6B-E, G-J). I used Spearman's rank correlation coefficient, which is a nonparametric measure of statistical correlation, instead of Pearson product-moment correlation coefficient for the comparisons, because there seemed to be outliers (Dixon's test, p for the efficacy in the same sign and the contribution in the opposite sign = 0.0091 and 0.0071, respectively) which may lead to artificial correlations.

Figure 2.6A shows comparisons of the efficacies between same- and opposite-response-sign pairs. There was no significant difference in the efficacy between the same- and the opposite-response-sign connections (median efficacy for same- and opposite-response-sign connections = 0.91 and 1.39, respectively; Wilcoxon rank sum test, p = 0.45), suggesting that the opposite-response-sign inputs were similarly efficient to the same-response-sign inputs. However, contrary to expectation, SHORT had an efficacy significantly smaller than LONG (median efficacy for SHORT and LONG = 0.37 and 1.25, respectively; Wilcoxon rank sum test, p = 0.019), indicating that the displaced inputs were more efficient. Furthermore, there was a significant negative correlation between the efficacy and the correlation coefficient of the RF structures in LONG (Figure 2.6E, black diamonds, ρ = -0.67, p = 0.028). These results suggest that, in LONG, connections with higher efficacies have less similar RF structures. Similarly, in the opposite sign, there was a significant positive

correlation between the efficacy and the inter-RF-centers distance (Figure 2.6C, gray dots, $\rho = 0.94$, $p = 0.017$), indicating that connections with higher efficacy share displaced RFs. In the remaining cases, no significant correlations were observed.

For the contribution, there were no significant differences between the response signs (Figure 2.6F, black symbols vs. gray dots, median contributions for the same and opposite signs = 1.62 and 2.14, respectively, Wilcoxon rank sum test, $p = 0.61$) or between SHORT and LONG (Figure 2.6F, black dots vs. black diamonds, median contributions for SHORT and LONG = 1.66 and 1.57, respectively, Wilcoxon rank sum test, $p = 0.88$). In SHORT, as expected, the contribution had a significant positive correlation with the correlation coefficient of the RF structures (Figure 2.6J, black dots, $\rho = 0.73$, $p = 0.031$), indicating that those with higher contribution share similar RFs. In LONG, there was a significant positive correlation between the contribution and the inter-RF-centers distance (Figure 2.6H, black diamonds, $\rho = 0.71$, $p = 0.019$). Again, the LONG connections with higher connection strength have less similar RF structures.

In addition, I investigated the relationships between the cell types of pairs (X RGC-X LGN neuron, X-Y, and Y-X; Table 2.1) and other measures (efficacy, contribution, difference in elongation angles, inter-RF-centers distance, overlap ratio, and correlation coefficient of RF structures). There were no significant differences in the measures among cell types of the pairs (Figure 2.7; efficacy, Kruskal-Wallis test, $\chi^2_{(2, 9)} = 0.22$, $p = 0.89$; contribution, $\chi^2_{(2, 9)} = 1.48$, $p = 0.48$; difference of elongation angles, $\chi^2_{(2, 9)} = 3.51$, $p = 0.17$; inter-RF-centers distance, $\chi^2_{(2, 9)} = 0.42$, $p = 0.81$; overlap ratio, $\chi^2_{(2, 9)} = 0.84$, $p = 0.66$; correlation coefficient of RF structures, $\chi^2_{(2, 9)} = 0.42$, $p = 0.81$). However, the populations seem too small (N for X-X, X-Y, and Y-X = 7, 3, and 2, respectively) to draw conclusive remarks.

Comparison of Temporal RF Structures of Connected Pairs

In the previous section, I found that the spatial RF structure of LGN neurons derives from two types of convergent inputs from RGCs. In this section, to clarify the underlying mechanisms for the generation of the temporal RF structure from the two types of convergent inputs, I calculated the temporal RF structures using SVD (see Methods), and then compared the structures between each retinogeniculate pair.

Figure 2.8 shows a representative example of a temporal RF structure of the LGN neuron shown in Figure 2.3. This neuron showed a strong OFF-response (see Figure 2.8A, inset second from left) with a short latency (first response), and then a weak ON-response (see Figure 2.8A, inset third from left) with a long latency (rebound). From the temporal RF structure, I extracted the peak latency of the first response (P1), peak latency of the rebound response (P2), duration of the first response (FWHM1), duration of the rebound response (FWHM2), and the relative amplitude of the rebound response to the first response (m). For example, for the LGN neuron in Figure 2.8A, P1, P2, FWHM1, FWHM2, and m were 55 ms, 96 ms, 27 ms, 70 ms, and -0.49, respectively. I then compared these values between the two cells of each retinogeniculate-connected pair to examine the possibility that the temporal RF structure of the LGN neurons is derived from the two types of convergent inputs from the RGCs.

Figure 2.9 shows comparisons of P1 (Figure 2.9A), FWHM1 (Figure 2.9B), P2 (Figure 2.9C), and FWHM2 (Figure 2.9D) between each pair. There were significant positive correlations or similar tendencies between each temporal property (P1, r for same and opposite response signs = 0.86 and 0.68, respectively, t-test of a correlation coefficient, $p = 6.6\times10^{-7}$ and = 0.068; FWHM1, r = 0.73 and 0.91, $p = 1.4\times10^{-4}$ and = 0.0066; P2, r = 0.58 and 0.82, p = 0.0036 and = 0.023; FWHM2, r = 0.42 and 0.70, p = 0.033 and = 0.062). These tendencies disappeared with the randomly sampled pairs (repeat count =

10000, r for P1, mean ± 1.96×SEM = -0.0030 ± 0.0039; FWHM1, -9.3×10^{-4} ± 0.0039; P2, -0.0017 ± 0.0039; FWHM2, -0.0019 ± 0.0039), indicating that a projecting RGC and its target LGN neuron exhibit similar temporal RF structures. These results suggest that the temporal RF structure of LGN neurons derives from the convergent inputs of two types of RGCs that have the same or opposite response sign of the spatial RF over different time courses.

Figure 2.9A also shows pairs in which a target LGN neuron has P1 equal to or shorter than that of its projecting RGC. In addition, in Figure 2.9B, LGN neurons show significantly longer FWHM1 than their projecting RGCs (medians for RGC and LGN neuron = 26 and 35, respectively, Wilcoxon signed-rank test, p = 0.0016). These results support the idea that there exist convergent retinogeniculate connections of various input latencies; the sum of multiple inputs of various latencies have a temporal range wider than the inputs (longer FWHM1), and in these cases, the latency of the sum is shorter for later inputs (shorter P1).

Discussions

In the current study, I simultaneously recorded the single-unit responses of RGCs and LGN neurons in cat and compared the spatiotemporal RF structures between neuron pairs monosynaptically connected. The results are summarized as follows: 1) RGCs exhibited elliptically elongated RF structures oriented in a direction toward the *area centralis*, and their aspect ratios (mean = 1.56, N = 168) were comparable to those of LGN neurons (mean = 1.62, N = 89); 2) for monosynaptically connected retinogeniculate pairs with RFs of the same response sign, the center regions of the two RFs were overlapped and oriented similarly; 3) for pairs with RFs of the opposite response sign, the center regions of the two RFs were spatially displaced and oriented independently; 4) for both populations of connected pairs, the RF spatial properties seemed to have relationships with the connection strength (efficacy and contribution); and 5) for both the populations, temporal RF structures were tightly correlated and the LGN neurons had significantly longer response durations than the RGCs. These results suggest that the spatiotemporal RF structure of a cat LGN neuron is mainly inherited from the dominant inputs of a projecting RGC, while convergent inputs from multiple RGCs may be responsible for enhancing its antagonistic center and surround regions.

Spatial RF Structure of RGCs

I found that RGCs exhibit an elliptical RF structure that is comparable to that seen in LGN neurons (Figures 2.1A and B). I also found that the spatial RF structures of the RGCs and LGN neurons were oriented in a direction toward the *area centralis* (Figures 2.1C and D).

My current results are consistent with previous studies reporting an elliptical spatial RF structure of cat RGCs (Rodieck and Stone, 1965; Hammond, 1974) and directional characteristic of RF elongation of cat LGN neurons (Vidyasagar and Urbas, 1982). Yet how the elongated RF structure of

RGCs is generated remains unclear. One possible explanation is that the RF structure reflects an anisotropic dendritic arborization of the RGCs. In fact, previous studies have reported that the dendritic fields of cat RGCs are elliptical (Boycott and Wässle, 1974; Leventhal and Schall, 1983) and oriented radially (Leventhal and Schall, 1983). Similarly, in primate, it has been reported that RGCs exhibit orientation selectivity (Passaglia et al., 2002) or radially-oriented dendritic field structures (Rodieck et al., 1985; Schall et al., 1986; Watanabe and Rodieck, 1989; Szmajda et al., 2005). On the other hand, in tree shrew, it is generally thought that orientation selective neurons first emerge in the visual cortex, especially layer 2/3 (Fitzpatrick, 1996; Bosking et al., 1997; Chisum et al., 2003; Veit et al., 2013; Scholl et al., 2013; Van Hooser et al., 2013), while only few neurons in the retina exhibit orientation selectivity (van Dongen et al., 1976; 6/93 neurons they recorded). Thus, these results suggest that the elliptically elongated RF structure of RGCs is an essential property despite species differences.

Retinogeniculate Connections and Response-Signs

I found that the majority of retinogeniculate-connected pairs exhibit same-response-sign RF structures (Figures 2.2, 2.3 and 2.5, 20/26 pairs), consistent with a previous study (Usrey et al., 1999). To my knowledge, there is little evidence that OFF (ON)-center RGCs project to ON (OFF)-center LGN neurons. Usrey et al. (1999) investigated the preference of the retinogeniculate connections in cat, reporting that one of twelve pairs had an opposite-response-sign RF. In the current study, I found six such pairs out of 26 pairs with retinogeniculate connections (Figures 2.2, 2.4 and 2.5). Thus, it is clear that LGN neurons receive both opposite-response-sign and same-response-sign inputs from RGCs.

My results strongly suggest that the opposite-response-sign inputs from the RGCs contribute to responses in the antagonistic RF surround region of the target LGN neurons. A similar model has been proposed by Hammond (1973) that describes a single LGN neuron receiving one same-response-sign

input and multiple opposite-response inputs, which correspond to the antagonistic center and surround region of the LGN neuron, respectively, from RGCs. The opposite-response-sign inputs may enhance the center-surround antagonism of the RF of the target LGN neurons compared to that of the projecting RGCs.

Neurons having spatial RF structures with stronger antagonism will exhibit more band-pass SF selectivity, because the center region has low-pass selectivity with a higher cut-off and the antagonistic surround region, which has low-pass selectivity with a lower cut-off, reduces responses to low-band SF stimuli. Cheng et al. (1995) investigated the SF selectivity of LGN neurons and projecting RGCs by recording S-potentials in cat LGN, demonstrating that the RGCs exhibited low-pass SF selectivity, while the target LGN neurons exhibited more band-pass SF selectivity. In addition, Kimura et al. (2013) investigated the SF selectivity of cat LGN neurons with bicuculline, a GABA receptor antagonist, reporting that neurons administered bicuculline iontophoretically exhibited more low-pass SF selectivity than those under the control condition. Thus, the antagonistic RF surround region of LGN neurons can be generated by both excitatory inputs from the RGCs and inhibitory inputs from local interneurons in the LGN and/or thalamic reticular nucleus.

Recently, Paik and Ringach (2011, 2012) suggested a model where the cortical orientation map takes origin from the retinal RF mosaic. More specifically, the retinal RF ON-OFF patterns, which are periodic but rotated and shifted with respect to one another, converge in the cortex, resulting in an orientation map of the cortex that has moiré interference patterns. My current results suggest that there are convergent inputs in the retinogeniculate connections, thus I can assume the same orientation map in the LGN. In fact, Shou and Leventhal (1989) investigated the relationship between the preferred orientations and RF positions of cat LGN neurons, finding that near neurons prefer similar orientations.

However, the orientation map in the cortex is unlikely to be directly inherited from the LGN because of geniculocortical convergent connections. Future studies are needed to clarify the relationships.

Another important finding was that a population of RGC-LGN pairs exhibited non-overlapped same-response-sign RFs (displaced same-response-sign projection, Figure 2.5B). It is possible that the non-overlapped same-response-sign and opposite-response-sign pairs are caused by pseudo projections from the RGCs. Rather than the simultaneously recorded RGC projecting to the LGN neuron, inter-retinally connected neighboring RGCs contributes to spike synchronization, which causes a non-overlapped or opposite-response-sign RF with the LGN neuron (Mastronarde, 1989) such that displaced inputs are the result of indirect connections. However, I found that connection strengths of neither input were lower than the near-placed same-sign inputs (Figures 2.6A and F). Thus, I conclude that the displaced projections are not indirect ones.

Another possibility is that the non-overlapped same-response-sign RFs were due to poor single unit isolation. Although I used strict criteria for single unit isolation as far as possible, the technical limitation did not allow me to completely eliminate the possibility of multi-unit recordings. If I recorded two RGCs with displaced RFs as a single unit, e.g. one RF overlapped with a target LGN RF and the other RF did not, the overlapped RF of RGC should also be reconstructed or extremely small efficacy/contribution values would be observed. Neither was observed in my results. In addition, the RFs of multi-unit activities will be larger than that of single-unit. However, I did not find such a trend (data not shown). Therefore, I concluded that it was unlikely that the non-overlapped same-response-sign RFs were due to poor single unit isolation.

Regardless, the functional significance of the displaced same-response-sign projection is not

clear. Several previous studies have reported that the RF size of LGN neurons is not fixed but varies depending on the stimulus contrast both in cat (Ozeki et al., 2004; Nolt et al., 2004; Bonin et al., 2005; Sadakane et al., 2006) and primate (Kremers et al., 2001; Solomon et al., 2002). Therefore, if the efficacy and/or contribution of the displaced same-response-sign projection to the RF spatial structure of LGN neurons depend on the stimulus contrast, the displaced same-response-sign projection may contribute to the contrast dependent RF size of LGN neurons. This point will be addressed in my future studies.

Efficacy and Contribution, and RF Property

I found that both efficacy and contribution were not significantly different between the same- and opposite-response-sign connections (Figures 2.6A and F). These results support my hypothesis that the opposite-response-sign inputs contribute to the generation of the antagonistic RF surround of the LGN neurons. My data also suggest that there are some relationships between the connection strength and the connection types: SHORT (same-response-sign connections with near-placed RFs) had higher contributions with similar RFs (Figure 2.6J), LONG (same-response-sign connection with displaced RFs) became stronger when they shared less similar and more displaced RFs (Figures 2.6E and H), and opposite-response-sign connections with more displaced RFs became stronger (Figure 2.6C).

Previous studies have reported that retinogeniculate connections with closer or more similar RFs become stronger (Mastronarde, 1992; Usrey et al., 1999), which agrees with my results on SHORT. However, there are no or few studies that report the LONG and opposite-response-sign connections. The strengths of these connections were variable, in contradiction to my expectation. These connections probably have functions different to SHORT. As described above, the opposite-response-sign connections possibly enhance the antagonistic RF surround of the LGN neurons. Thus, the connections

may be weighed in proportion to the inter-RF-centers distances; inputs near the RF center of the LGN neurons should be weak, and those far should be strong. Similarly, LONG may contribute to the contrast dependency of the size tuning exhibited in the LGN. To achieve this function, it may be efficient for LONG to have displaced and dissimilar RFs.

Temporal RF Structures of Retinogeniculate-Connected Pairs

I found that projecting RGCs and their target LGN neurons exhibit similar temporal RF structures and that there seems to exist temporally-varied convergent inputs in retinogeniculate connections (Figures 2.9A and B). Hamamoto et al. (1994) investigated the TF selectivity of target LGN neurons and the corresponding projecting RGCs by recording S-potentials in cat LGN, finding that LGN neurons exhibited sharper band-pass TF selectivity than the projecting RGCs. Thus, these temporally-varied convergent inputs can facilitate temporal summation and induce a sharpening of the TF selectivity in connected neurons.

To summarize, LGN neurons have a spatiotemporal RF structure that have, compared to projecting RGCs similarly elongated, enhanced antagonistic surround and longer duration of response. In other words, LGN neurons can exhibit similar orientation selectivity, but sharper band-pass SF and TF selectivity compared to their projecting RGCs. My results suggest that the orientation selectivity of LGN neurons is inherited from its primary projecting RGC, and the sharpened SF and TF selectivities are induced by convergent retinogeniculate connections. These connections can induce the staged visual image processing in the early visual system. Moreover, the resultant preferences may be inherited or enhanced in the visual cortex by geniculocortical convergent connections when the geniculate neurons projecting to a particular cortical neuron have the similar preferences. In a natural scene, there exist various sources of SF information such as low SF in the sky, middle SF in the contour of wood, and high

SF in the textures of the road, and also various sources of TF information such as low TF in still life, middle TF in moving animals, and high TF in flickering light. Thus, retinogeniculate connections may conduct important visual image processing tasks that detect proper information while at the same time reducing noise.

Figures

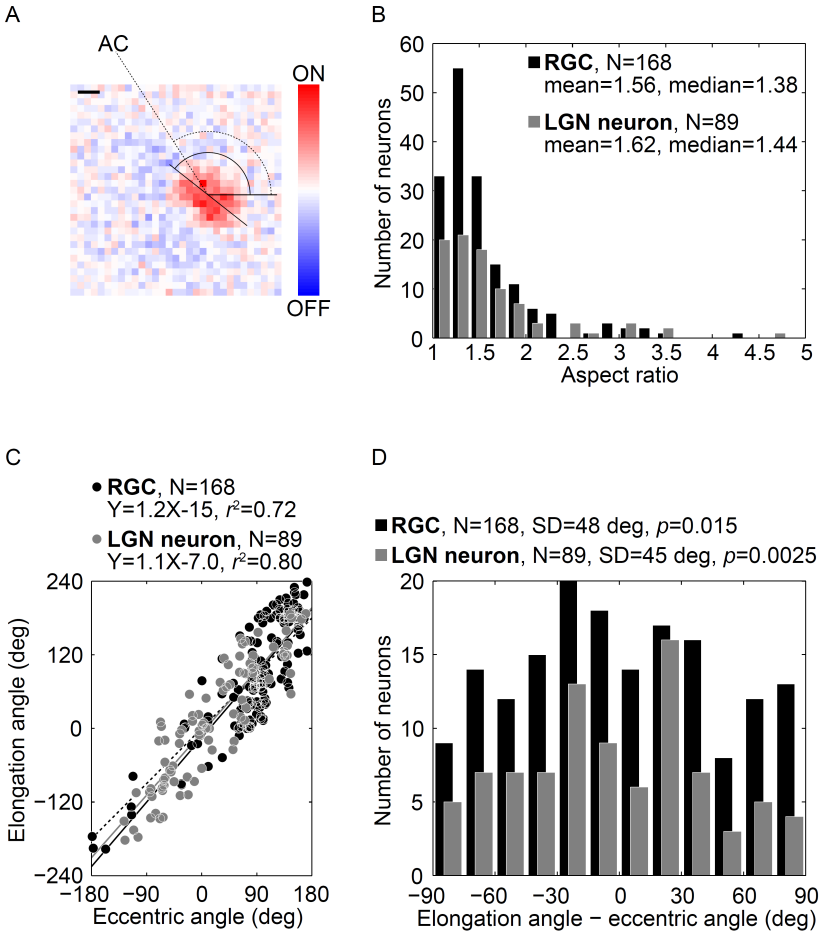

Figure 2.1: Comparison of RF structures of RGCs and LGN neurons. A) Example of a RF structure of an ON-center RGC at the peak response latency (40 ms). Reddish and bluish colors indicate ON- and OFF-responses, respectively. The aspect ratio, elongation angle (solid arc) of the center region, and eccentric angle (dotted arc) were 1.38, 142 deg, and 123 deg, respectively. AC indicates the *area centralis*. Scale bar = 1 deg. B–D) Distributions of the aspect ratios (B), relationship between the elongation and eccentric angles (see details in text) (C), and distributions of differences between elongation and eccentric angles (D). Black and gray bars/circles indicate RGCs and LGN neurons, respectively.

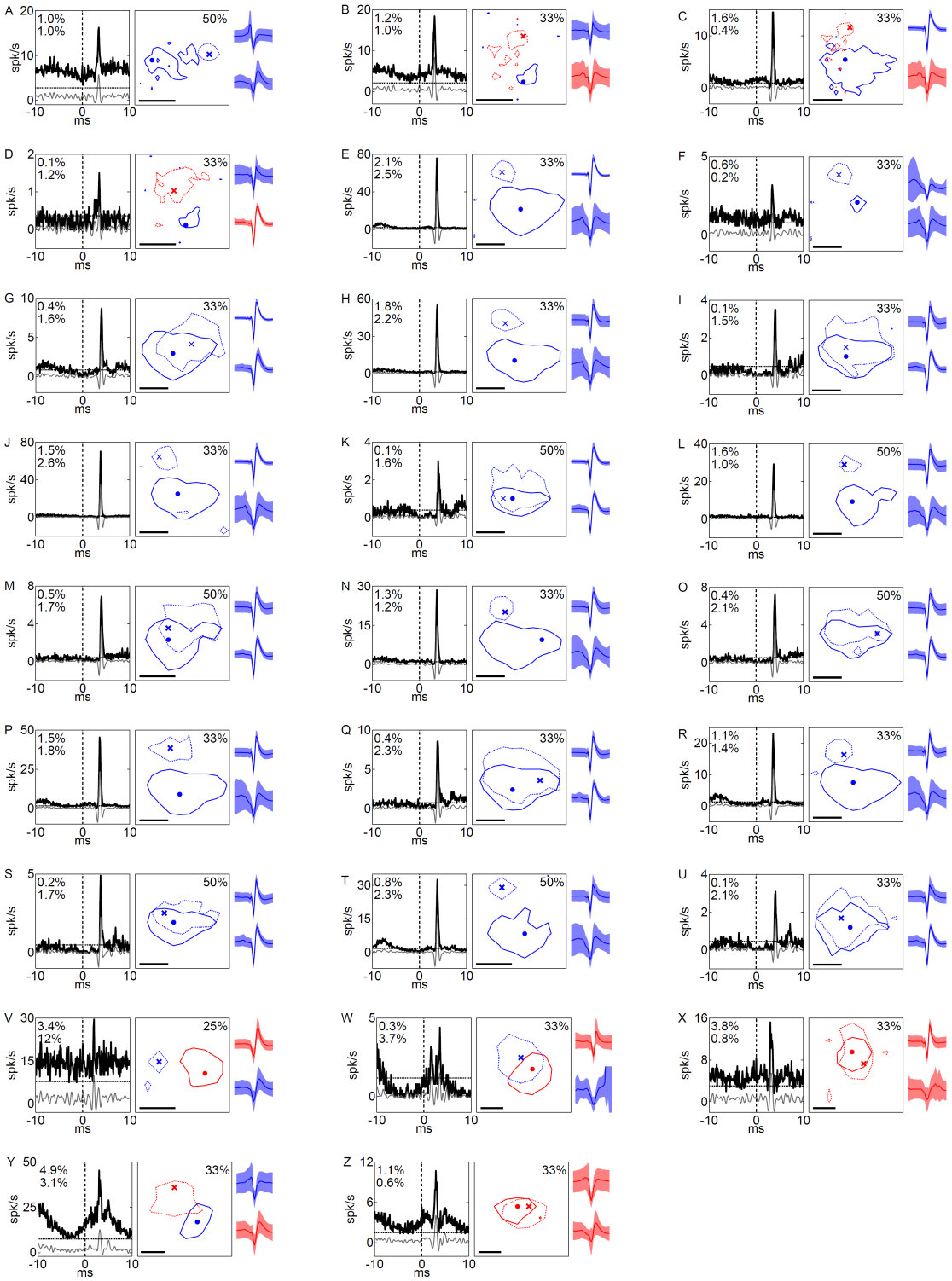
A
1.0%
1.0%
50%
B
1.2%
1.0%
33%
C
1.6%
0.4%
33%
D
0.1%
1.2%
33%
E
2.1%
2.5%
33%
F
0.6%
0.2%
33%
G
0.4%
1.6%
33%
H
1.8%
2.2%
33%
I
0.1%
1.5%
33%
J
1.5%
2.6%
33%
K
0.1%
1.6%
50%
L
1.6%
1.0%
50%
M
0.5%
1.7%
50%
N
1.3%
1.2%
33%
O
0.4%
2.1%
50%
P
1.5%
1.8%
33%
Q
0.4%
2.3%
33%
R
1.1%
1.4%
33%
S
0.2%
1.7%
50%
T
0.8%
2.3%
50%
U
0.1%
2.1%
33%
V
3.4%
12%
25%
W
0.3%
3.7%
33%
X
3.8%
0.8%
33%
Y
4.9%
3.1%
33%
Z
1.1%
0.6%
33%
spk/s
ms

Figure 2.2: Summary of RFs and corresponding XCs for all pairs. In each sub-figure, left, middle, and right columns indicate XC, RF, and spike shape, respectively. In the XC columns, black solid, gray solid, and horizontal dotted lines indicate raw XC, filtered XC, and threshold (mean + 5 SD), respectively, and numbers read efficacy (upper) and contribution (lower). In RF columns, solid and dotted lines indicate the RFs of the RGC and the LGN neuron, respectively. Numbers read the response levels of the contour lines for the both of units. Dot and cross symbols indicate the maximum response positions of the RGC and the LGN neuron, respectively. Scale bar = 1 deg. In spike shape columns, solid lines and shaded areas indicate mean and 1 SD, respectively. Colors correspond to the response sign (red, ON; blue, OFF). Upper and lower shapes are for an RGC and LGN neuron, respectively. Pairs in Figures 2.3 and 2.4 correspond to S and C, respectively. B and C are reconstructed from the same recording and exhibited the same LGN neuron with different RGCs, indicating two OFF-center RGCs were projecting to one ON-center LGN neuron.

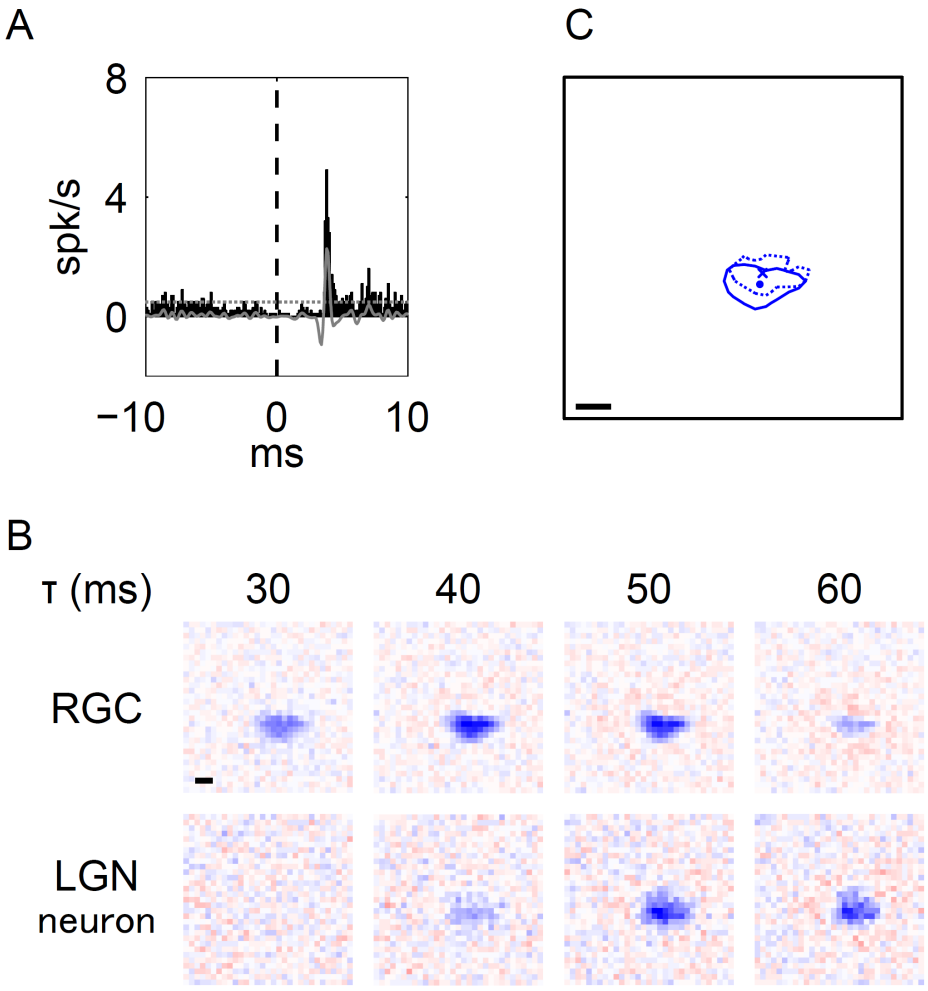

Figure 2.3: Typical example of an RGC-LGN neuron pair with RFs of the same response sign. This was the pair shown in Figure 2.2S. A) XC of the pair. Black bars and gray line indicate raw and filtered data, respectively. Horizontal dotted line indicates mean + 5 SD. B) Spatiotemporal RF structures (top: RGC, bottom: LGN neuron; left to right: shorter to longer latencies). C) Overlaid image of the RF centers. Solid line and dot indicate 50% of response level and center position of the RGC, respectively. Dotted line and cross-symbol indicate those of the LGN neuron. The RF center positions were obtained from the fitted parameters. In B) and C), scale bar = 1 deg.

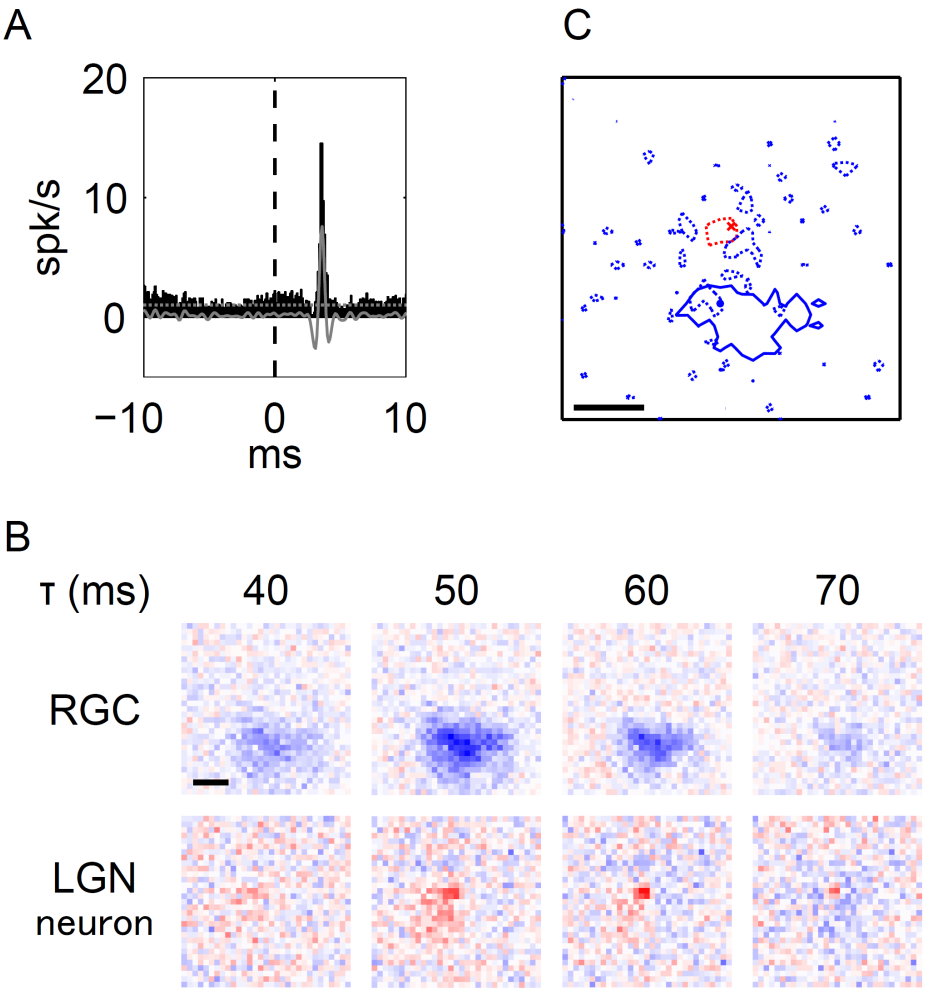

Figure 2.4: Typical example of an RGN-LGN neuron pair with RFs of the opposite response sign. This was the pair shown in Figure 2.2C. Details are the same as Figure 2.3. Note that the blue dotted lines in C indicate the RF surround of the LGN neuron at 25% response level at latency 70 ms.

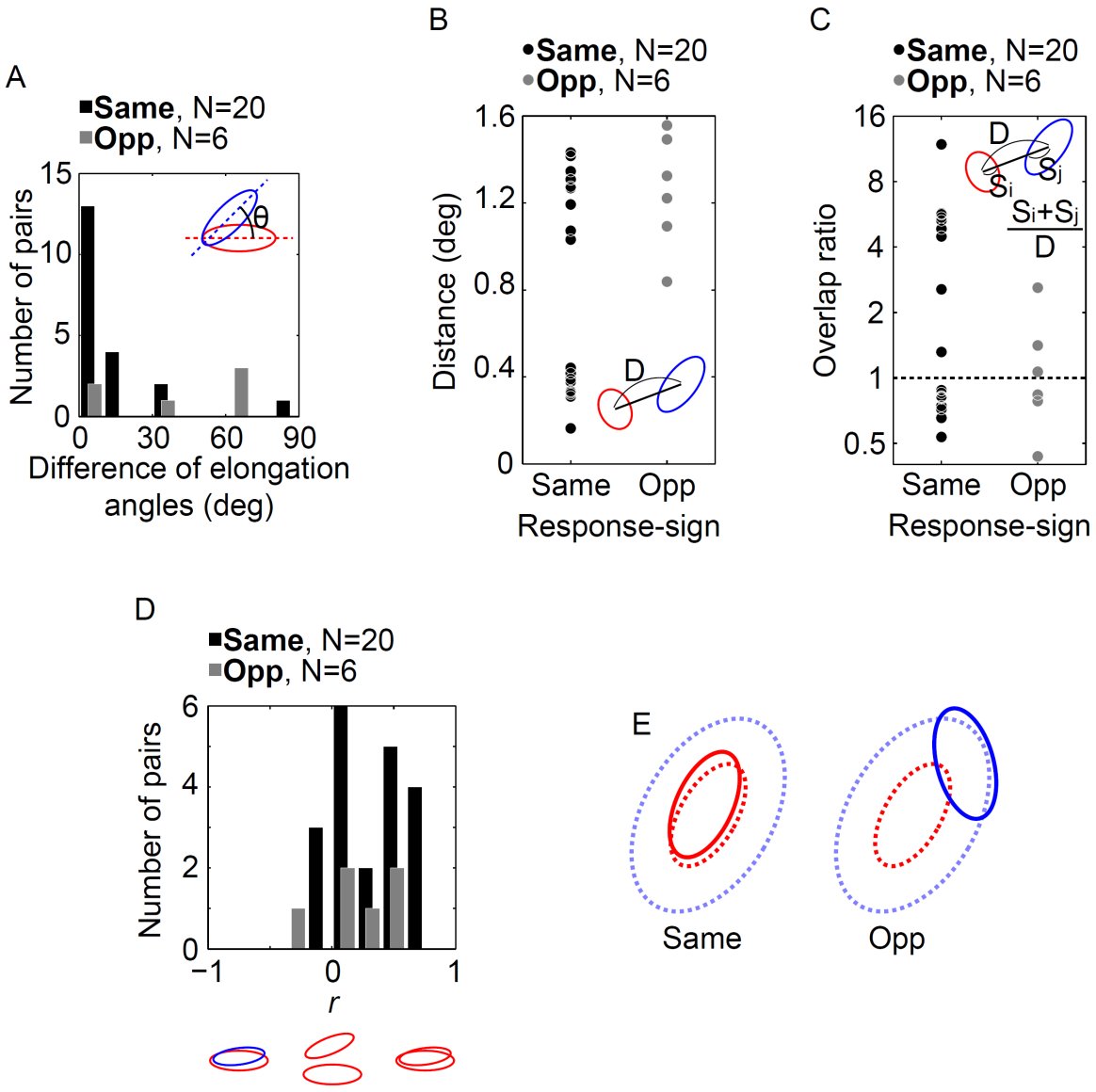

Figure 2.5: Relationship between the spatial RF structures of retinogeniculate-connected pairs (N = 26). A) Distributions of the difference of elongation angles of the spatial RF structures. B) Distributions of RF center distances of the pairs. C) Distributions of the overlap ratios between the antagonistic RF center regions of the pairs. D) Distributions of *r* between the spatial RF structures of the pairs. An RGC-LGN neuron pair exhibit completely overlapped RF structures with the same response sign when *r*

= 1 and completely overlapped RF structures with the opposite response sign when r = -1. In A) to D), insets indicate schematic spatial RF structures. θ, D, S indicate the difference of elongation angles, distance between RF center positions, and size of spatial RF structure, respectively. Black and gray bars/circles indicate pairs with RFs of the same (N = 20) and opposite response sign (N = 6), respectively. E) Schematic summary of spatial RF structures in the retinogeniculate connections. Solid and dotted lines indicate spatial RF structures of RGCs and the corresponding target LGN neurons, respectively. In same- and opposite-response-sign pairs, RGCs exhibit ON-center and OFF-center RFs, respectively. In both pairs, LGN neuron exhibits ON-center OFF-surround RF.

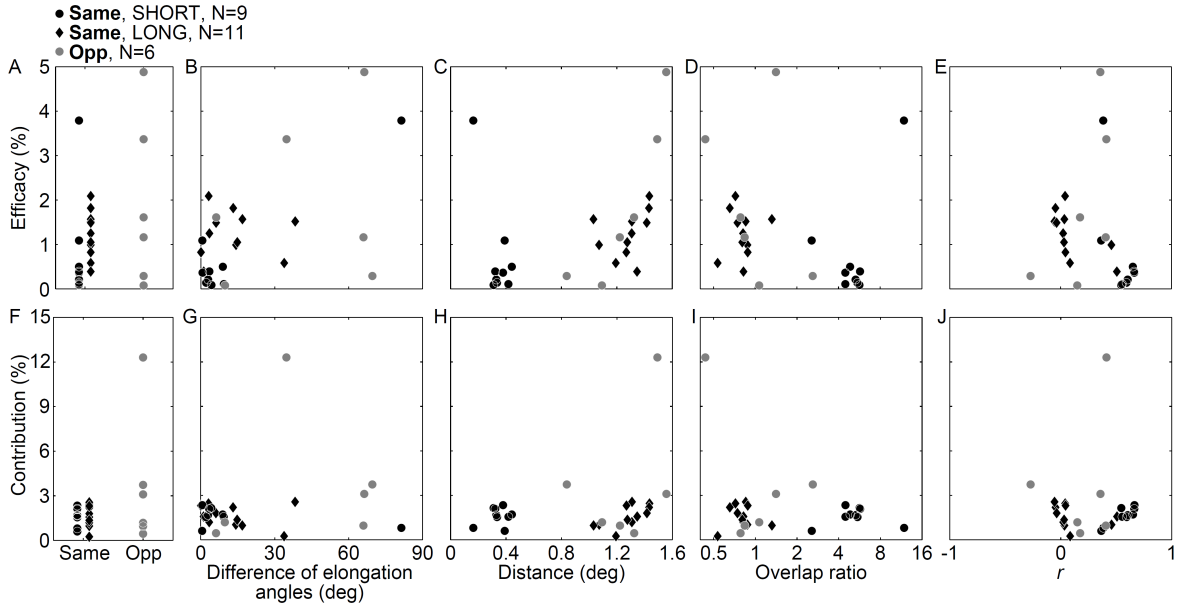

Figure 2.6: Efficacy and contribution, and the correlations with RF properties. In the upper row, the efficacy itself (A), correlations with the difference of the elongation angles (B), distance between RF center positions (C), overlap ratio (D), and correlation coefficient of the RF structures (E) are shown. In the lower row, the contribution itself (F), correlations with differences of elongation angles (G), distance between RF center positions (H), overlap ratio (I), and correlation coefficient of the RF structures (J) are shown. Black dots, black diamonds, and gray dots indicate SHORT, LONG, and opposite-response-sign connections, respectively.

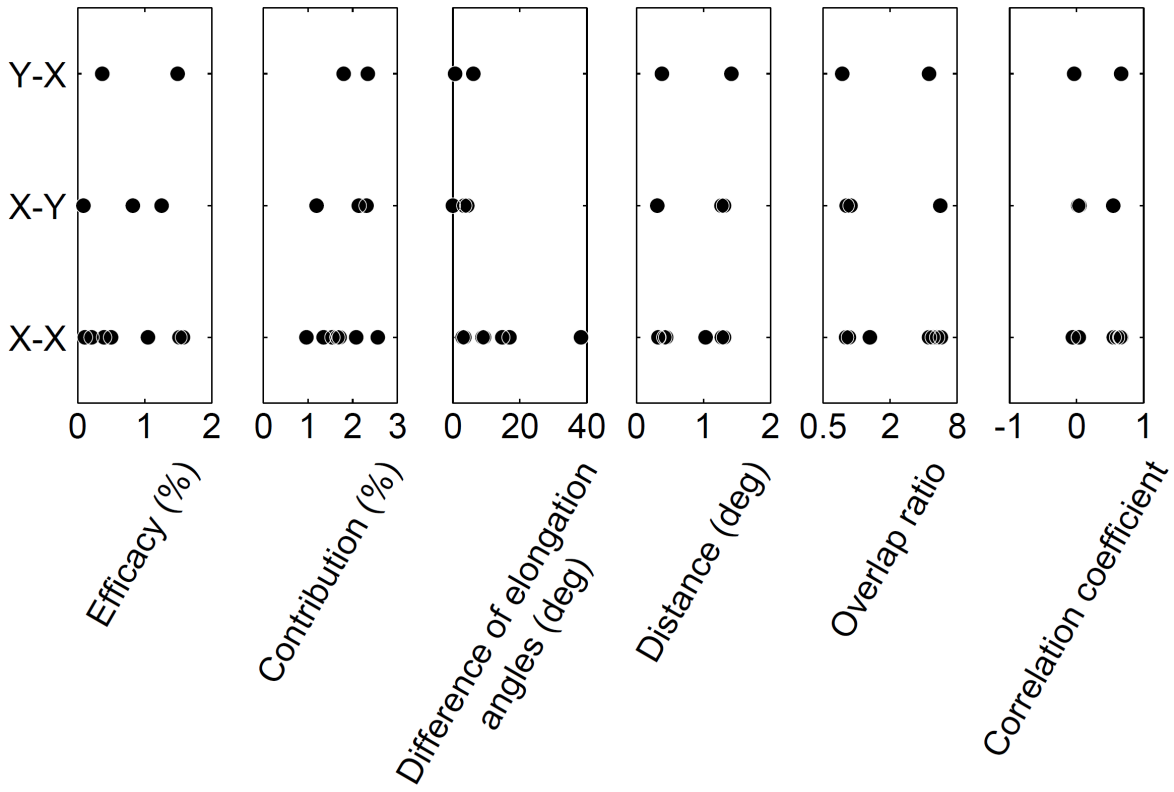

Figure 2.7: Relationships between cell types and RF properties. From left to right, the relationships between the cell types in connection (X-X, X-Y, and Y-X) and efficacy, contribution, difference of elongation angles, inter-RF-centers distance, overlap ratio, and correlation coefficient of RF structures are shown. Note that the range of some abscissae is different to those in Figures 2.6 and 2.7 for ease of viewing.

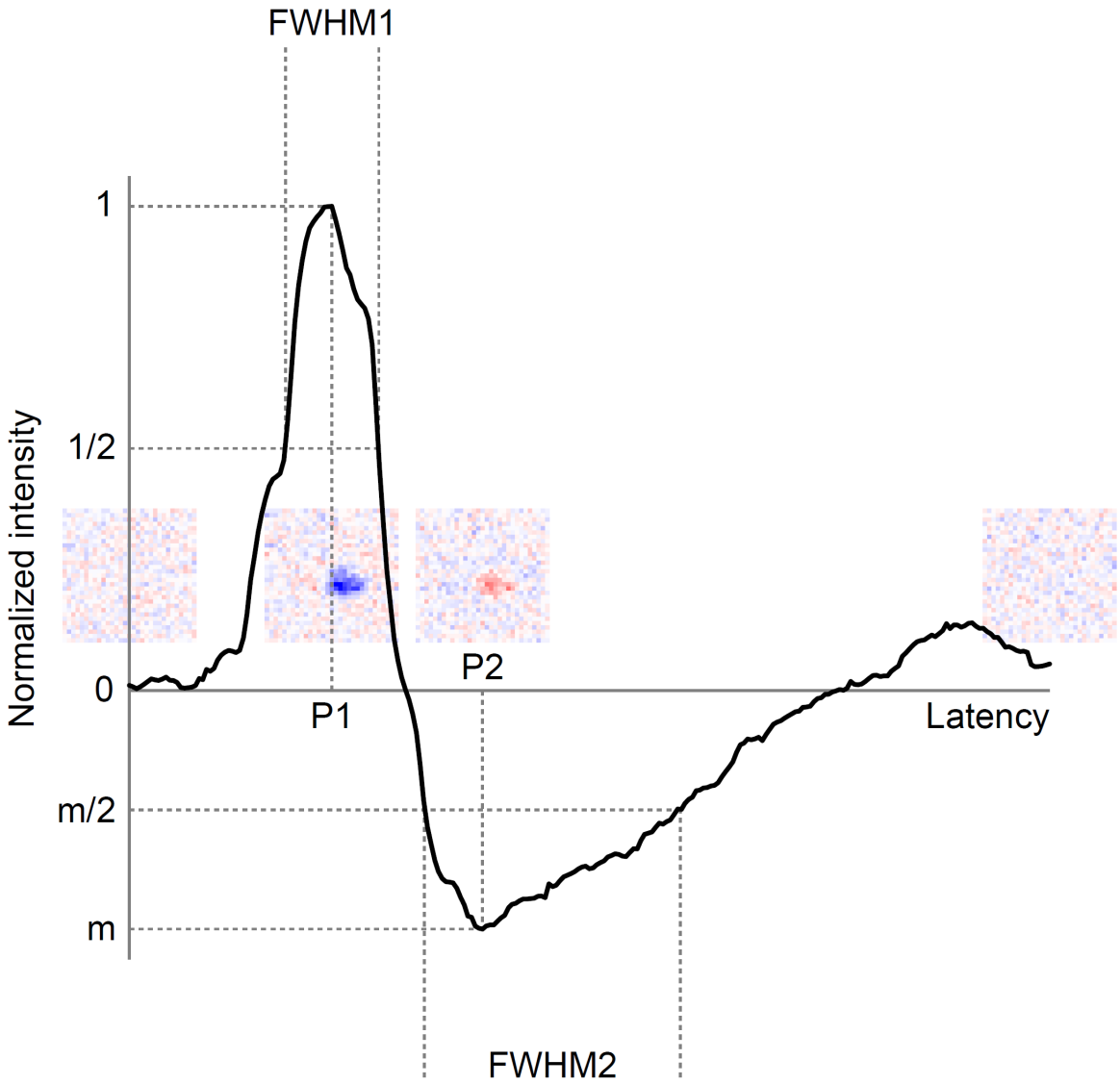

Figure 2.8: Typical example of the temporal RF structure of LGN neurons. Horizontal and vertical axes indicate latency and normalized intensity of the temporal RF structure, respectively. P1, P2, FWHM1, FWHM2, and m indicate peak latency of the first response, peak latency of the rebound response, duration of the first response, duration of the rebound response, and relative amplitude of the rebound response, respectively. Insets indicate spatial RF structures at latencies of 0, 55 (P1), 96 (P2), 250 ms, respectively.

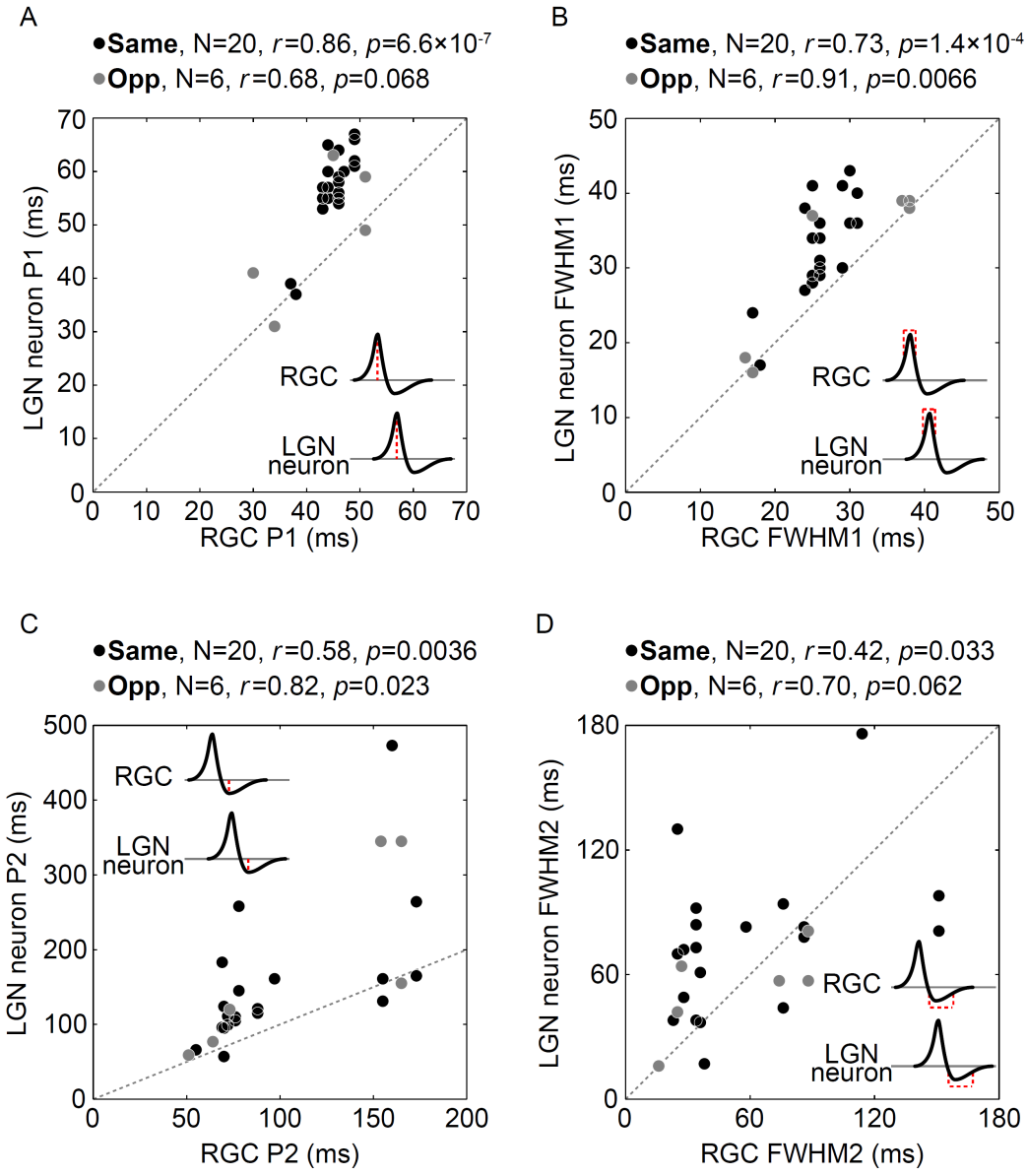

Figure 2.9: Relationship between temporal RF structures of retinogeniculate-connected pairs. Relationship between P1 (A), FWHM1 (B), P2 (C), and FWHM2 (D) for RGCs (horizontal axis) and LGN neurons (vertical axis). Black and gray circles indicate same- and opposite-response-sign pairs, respectively. Insets indicate schematic temporal RF structures. Note that the scale of the horizontal axis and that of the vertical axis are not equal in C).

References

Ahmed, B., and Hammond, P. (1991). Orientation bias of cat dorsal lateral geniculate cells: directional analysis of the major axis of the receptive field centre. *Exp. Brain Res.* 84, 676–9. doi: 10.1007/BF00230982.

Alonso, J.-M., Yeh, C.-I., Weng, C., and Stoelzel, C. (2006). Retinogeniculate connections: A balancing act between connection specificity and receptive field diversity. *Prog. Brain Res.* 154, 3–13. doi: 10.1016/S0079-6123(06)54001-4.

Bonin, V., Mante, V., and Carandini, M. (2005). The suppressive field of neurons in lateral geniculate nucleus. *J. Neurosci.* 25, 10844–56. doi: 10.1523/JNEUROSCI.3562-05.2005.

Bosking, W. H., Zhang, Y., Schofield, B., and Fitzpatrick, D. (1997). Orientation selectivity and the arrangement of horizontal connections in tree shrew striate cortex. *J. Neurosci.* 17, 2112–27.

Boycott, B., and Wässle, H. (1974). The morphological types of ganglion cells of the domestic cat's retina. *J. Physiol.* 240, 397–419.

Brainard, D. (1997). The psychophysics toolbox. *Spat. Vis.* 10, 433–6.

Campbell, F., Cooper, G., and Enroth-Cugell, C. (1969). The spatial selectivity of the visual cells of the cat. *J. Physiol.* 203, 223–35.

Cheng, H., Chino, Y., Smith III, E., Hamamoto, J., and Yoshida, K. (1995). Transfer characteristics of lateral geniculate nucleus X neurons in the cat: effects of spatial frequency and contrast. *J. Neurophysiol.*, 2548–2557.

Cheong, S. K., Tailby, C., Solomon, S. G., and Martin, P. R. (2013). Cortical-like receptive fields in the lateral geniculate nucleus of marmoset monkeys. *J. Neurosci.* 33, 6864–76. doi: 10.1523/JNEUROSCI.5208-12.2013.

Chisum, H. J., Mooser, F., and Fitzpatrick, D. (2003). Emergent properties of layer 2/3 neurons reflect the collinear arrangement of horizontal connections in tree shrew visual cortex. *J. Neurosci.* 23, 2947–60.

Derrington, A. M., and Fuchs, A. F. (1979). Spatial and temporal properties of X and Y cells in the cat lateral geniculate nucleus. *J. Physiol.* 293, 347–64.

Van Dongen, P. A., ter Laak, H. J., Thijssen, J. M., and Vendrik, A. J. (1976). Functional classification of cells in the optic tract of a tree shrew (Tupaia chinensis). *Exp. Brain Res.* 24, 441–6.

Enroth-Cugell, C., and Robson, J. G. (1966). The contrast sensitivity of retinal ganglion cells of the cat. *J. Physiol.* 187, 517–52.

Fitzpatrick, D. (1996). The functional organization of local circuits in visual cortex: insights from the study of tree shrew striate cortex. *Cereb. Cortex* 6, 329–41.

Frishman, L. J., Freeman, A. W., Troy, J. B., Schweitzer-Tong, D. E., and Enroth-Cugell, C. (1987). Spatiotemporal frequency responses of cat retinal ganglion cells. *J. Gen. Physiol.* 89, 599–628.

Fukuda, Y., and Stone, J. (1974). Retinal distribution and central projections of Y-, X-, and W-cells of the cat's retina. *J. Neurophysiol.* 37, 749–72.

Hamamoto, J., Cheng, H., Yoshida, K., Smith, E., and Chino, Y. (1994). Transfer characteristics of lateral geniculate nucleus X-neurons in the cat: effects of temporal frequency. *Exp. Brain Res.* 98, 191–9. doi: 10.1007/BF00228408.

Hammond, P. (1974). Cat retinal ganglion cells: size and shape of receptive field centres. *J. Physiol.* 242, 99–118.

Hammond, P. (1973). Contrasts in spatial organization of receptive fields at geniculate and retinal levels: centre, surround and outer surround. *J. Physiol.* 228, 115–37.

Hochstein, S., and Shapley, R. M. (1976). Quantitative analysis of retinal ganglion cell classifications. *J. Physiol.* 262, 237–64.

Van Hooser, S. D., Roy, A., Rhodes, H. J., Culp, J. H., and Fitzpatrick, D. (2013). Transformation of receptive field properties from lateral geniculate nucleus to superficial V1 in the tree shrew. *J. Neurosci.* 33, 11494–505. doi: 10.1523/JNEUROSCI.1464-13.2013.

Hubel, D. H., and Wiesel, T. N. (1977). Functional architecture of macaque monkey visual cortex. *Proc. R. Soc. London. Ser. B. Biol. Sci.* 198, 1.

Hubel, D. H., and Wiesel, T. N. (1959). Receptive fields of single neurones in the cat's striate cortex. *J. Physiol.* 148, 574–91.

Hubel, D. H., and Wiesel, T. N. (1962). Receptive fields, binocular interaction and functional architecture in the cat's visual cortex. *J. Physiol.* 160, 106–154.

Jones, J., and Palmer, L. (1987). The two-dimensional spatial structure of simple receptive fields in cat striate cortex. *J. Neurophysiol.*, 1187–1211.

Kimura, A., Shimegi, S., Hara, S., Okamoto, M., and Sato, H. (2013). Role of GABAergic inhibition in shaping the spatial frequency tuning of neurons and its contrast dependency in the dorsal lateral geniculate nucleus of cat. *Eur. J. Neurosci.* 37, 1270–83. doi: 10.1111/ejn.12149.

Kremers, J., Silveira, L. C. L., and Kilavik, B. E. (2001). Influence of contrast on the responses of marmoset lateral geniculate cells to drifting gratings. *J Neurophysiol* 85, 235–246.

Leventhal, A. G., and Schall, J. D. (1983). Structural basis of orientation sensitivity of cat retinal ganglion cells. *J. Comp. Neurol.* 220, 465–75. doi: 10.1002/cne.902200408.

Mastronarde, D. N. (1989). Correlated firing of retinal ganglion cells. *Trends Neurosci.* 12, 75–80. doi: 10.1016/0166-2236(89)90140-9.

Mastronarde, D. N. (1992). Nonlagged relay cells and interneurons in the cat lateral geniculate nucleus: receptive-field properties and retinal inputs. *Vis. Neurosci.* 8, 407–41. doi: 10.1017/S0952523800004934.

Mihashi, T., Okawa, Y., Miyoshi, T., Kitaguchi, Y., Hirohara, Y., and Fujikado, T. (2011). Comparing retinal reflectance changes elicited by transcorneal electrical retinal stimulation with those of optic chiasma stimulation in cats. *Jpn. J. Ophthalmol.* 55, 49–56. doi: 10.1007/s10384-010-0906-x.

Moore, B. D., Kiley, C. W., Sun, C., and Usrey, W. M. (2011). Rapid plasticity of visual responses in the adult lateral geniculate nucleus. *Neuron* 71, 812–9. doi: 10.1016/j.neuron.2011.06.025.

Movshon, J. A., Thompson, I. D., and Tolhurst, D. J. (1978). Spatial and temporal contrast sensitivity of neurones in areas 17 and 18 of the cat's visual cortex. *J. Physiol.* 283, 101–20.

Naito, T., Okamoto, M., Sadakane, O., Shimegi, S., Osaki, H., Hara, S.-I., Kimura, A., Ishikawa, A., Suematsu, N., and Sato, H. (2013). Effects of stimulus spatial frequency, size, and luminance contrast on orientation tuning of neurons in the dorsal lateral geniculate nucleus of cat. *Neurosci. Res.* doi: http://dx.doi.org/10.1016/j.neures.2013.08.009.

Naito, T., Sadakane, O., Okamoto, M., and Sato, H. (2007). Orientation tuning of surround suppression in lateral geniculate nucleus and primary visual cortex of cat. *Neuroscience* 149, 962–75. doi: 10.1016/j.neuroscience.2007.08.001.

Niell, C. M. (2013). Vision: more than expected in the early visual system. *Curr. Biol.* 23, R681–4. doi: 10.1016/j.cub.2013.07.049.

Nolt, M. J., Kumbhani, R. D., and Palmer, L. A. (2004). Contrast-dependent spatial summation in the lateral geniculate nucleus and retina of the cat. *J. Neurophysiol.* 92, 1708–17. doi: 10.1152/jn.00176.2004.

Ozeki, H., Sadakane, O., Akasaki, T., Naito, T., Shimegi, S., and Sato, H. (2004). Relationship between excitation and inhibition underlying size tuning and contextual response modulation in the cat primary visual cortex. *J. Neurosci.* 24, 1428–38. doi: 10.1523/JNEUROSCI.3852-03.2004.

Paik, S.-B., and Ringach, D. L. (2012). Link between orientation and retinotopic maps in primary visual cortex. *Proc. Natl. Acad. Sci.* 109, 7091–6. doi: 10.1073/pnas.1118926109.

Paik, S.-B., and Ringach, D. L. (2011). Retinal origin of orientation maps in visual cortex. *Nat. Neurosci.* 14, 919–25. doi: 10.1038/nn.2824.

Passaglia, C. L., Troy, J. B., Rüttiger, L., and Lee, B. B. (2002). Orientation sensitivity of ganglion cells in primate retina. *Vision Res.* 42, 683–694. doi: 10.1016/S0042-6989(01)00312-1.

Pelli, D. G. (1997). The VideoToolbox software for visual psychophysics: transforming numbers into movies. *Spat. Vis.* 10, 437–442. doi: 10.1163/156856897X00366.

Quiroga, R. Q., Nadasdy, Z., and Ben-Shaul, Y. (2004). Unsupervised spike detection and sorting with wavelets and superparamagnetic clustering. *Neural Comput.* 16, 1661–87. doi: 10.1162/089976604774201631.

Rodieck, R. W., Binmoeller, K. F., and Dineen, J. (1985). Parasol and midget ganglion cells of the human retina. *J. Comp. Neurol.* 233, 115–32. doi: 10.1002/cne.902330107.

Rodieck, R. W., and Stone, J. (1965). Analysis of receptive fields of cat retinal ganglion cells. *J. Neurophysiol.* 28, 832–49.

Sadakane, O., Ozeki, H., Naito, T., Akasaki, T., Kasamatsu, T., and Sato, H. (2006). Contrast-dependent, contextual response modulation in primary visual cortex and lateral geniculate nucleus of the cat. *Eur. J. Neurosci.* 23, 1633–42. doi: 10.1111/j.1460-9568.2006.04681.x.

Schall, J. D., Perry, V. H., and Leventhal, A. G. (1986). Retinal ganglion cell dendritic fields in old-world monkeys are oriented radially. *Brain Res.* 368, 18–23. doi: 10.1016/0006-8993(86)91037-1.

Scholl, B., Tan, A. Y. Y., Corey, J., and Priebe, N. J. (2013). Emergence of orientation selectivity in the Mammalian visual pathway. *J. Neurosci.* 33, 10616–24. doi: 10.1523/JNEUROSCI.0404-13.2013.

Shou, T., and Leventhal, A. G. (1989). Organized arrangement of orientation-sensitive relay cells in the cat's dorsal lateral geniculate nucleus. *J. Neurosci.* 9, 4287–4302.

Smith, E. L., Chino, Y. M., Ridder, W. H., Kitagawa, K., and Langston, A. (1990). Orientation bias of neurons in the lateral geniculate nucleus of macaque monkeys. *Vis. Neurosci.* 5, 525–45.

Solomon, S. G., White, A. J. R., and Martin, P. R. (2002). Extraclassical Receptive Field Properties of Parvocellular, Magnocellular, and Koniocellular Cells in the Primate Lateral Geniculate Nucleus. *J. Neurosci.* 22, 338–349.

Soodak, R. E., Shapley, R. M., and Kaplan, E. (1987). Linear mechanism of orientation tuning in the retina and lateral geniculate nucleus of the cat. *J. Neurophysiol.* 58, 267–75.

Stone, J., and Fukuda, Y. (1974). Properties of cat retinal ganglion cells: a comparison of W-cells with X- and Y-cells. *J. Neurophysiol.* 37, 722–48.

Suematsu, N., Naito, T., and Sato, H. (2012). Relationship between orientation sensitivity and spatiotemporal receptive field structures of neurons in the cat lateral geniculate nucleus. *Neural Networks* 35, 10–20. doi: 10.1016/j.neunet.2012.06.008.

Szmajda, B. A., Grünert, U., and Martin, P. R. (2005). Mosaic properties of midget and parasol ganglion cells in the marmoset retina. *Vis. Neurosci.* 22, 395–404. doi: 10.1017/S0952523805224021.

Takao, M., Miyoshi, T., Watanabe, M., and Fukuda, Y. (2002). Changes in visual response properties of cat retinal ganglion cells within two weeks after axotomy. *Exp. Neurol.* 177, 171–182. doi: 10.1006/exnr.2002.7958.

Takao, M., Wang, Y., Miyoshi, T., Fujita, I., and Fukuda, Y. (2000). A new intraretinal recording system with multiple-barreled electrodes for pharmacological studies on cat retinal ganglion cells. *J. Neurosci. Methods* 97, 87–92. doi: 10.1016/S0165-0270(00)00171-0.

Tavazoie, S. F., and Reid, R. C. (2000). Diverse receptive fields in the lateral geniculate nucleus during thalamocortical development. *Nat. Neurosci.* 3, 608–16. doi: 10.1038/75786.

Usrey, W. M., Reppas, J. B., and Reid, R. C. (1999). Specificity and strength of retinogeniculate connections. *J. Neurophysiol.* 82, 3527–40.

Veit, J., Bhattacharyya, A., Kretz, R., and Rainer, G. (2013). On the relation between receptive field structure and stimulus selectivity in the tree shrew primary visual cortex. *Cereb. Cortex*. doi: 10.1093/cercor/bht133.

Vidyasagar, T. R., and Urbas, J. V (1982). Orientation sensitivity of cat LGN neurones with and without inputs from visual cortical areas 17 and 18. *Exp. Brain Res.* 46, 157–69.

Watanabe, M., and Rodieck, R. W. (1989). Parasol and midget ganglion cells of the primate retina. *J. Comp. Neurol.* 289, 434–54. doi: 10.1002/cne.902890308.

Wolfe, J., and Palmer, L. A. (1998). Temporal diversity in the lateral geniculate nucleus of cat. *Vis. Neurosci.* 15, 653–75.

Zhao, X., Chen, H., Liu, X., and Cang, J. (2013). Orientation-selective responses in the mouse lateral geniculate nucleus. *J. Neurosci.* 33, 12751–63. doi: 10.1523/JNEUROSCI.0095-13.2013.

Conclusions

In this doctoral thesis, I investigated the relationship between the spatial RF structures and the orientation tunings in cat LGN, and the relationship between the spatiotemporal RF structures and the fashion of retinogeniculate projections. My results suggest that subcortical visual pathway conducts more complex visual information processing than ever thought. Further studies should be conducted to clarify the dynamic condributions of the subcortical visual information processing on the higher stages of the visual pathway.

Acknowledgements

The author thanks to Drs. Ichiro Fujita, Izumi Ohzawa, Shigeru Kitazawa and Hiromichi Sato for their helpful comments, to Drs. Tomoyuki Naito, Tomomitsu Miyoshi and Hajime Sawai for their technical supports, and to all other members of my laboratory for their assistance and supports.

Research Achievements

Original Paper

Suematsu, N., Naito, T., & Sato, H. (2012). Relationship between orientation sensitivity and spatiotemporal receptive field structures of neurons in the cat lateral geniculate nucleus. *Neural Netw.* 35, 10–20. doi: 10.1016/j.neunet.2012.06.008

Soma, S., Shimegi, S., Suematsu, N., & Sato, H. (2013). Cholinergic modulation of response gain in the rat primary visual cortex. *Sci. Rep.* 3, 1138. doi: 10.1038/srep01138

Soma, S., Shimegi, S., Suematsu, N., Tamura, H., & Sato, H. (2013). Modulation-specific and laminar-dependent effects of acetylcholine on visual responses in the rat primary visual cortex. *PLOS ONE*, 8(7), e68430. doi: 10.1371/journal.pone.0068430

Naito, T., Okamoto, M., Sadakane, O., Shimegi, S., Osaki, H., Hara, S.-I., Kimura, A., Ishikawa, A., Suematsu, N., Sato, H. (2013). Effects of stimulus spatial frequency, size, and luminance contrast on orientation tuning of neurons in the dorsal lateral geniculate nucleus of cat. *Neurosci. Res.* 77(3), 143–54. doi: 10.1016/j.neures.2013.08.009

Soma, S., Suematsu, N., & Shimegi, S. (2013). Cholinesterase inhibitor, donepezil, improves visual contrast detectability in freely behaving rats. *Behav. Brain Res.* 256, 362–7. doi: 10.1016/j.bbr.2013.08.022

Suematsu, N., Naito, T., Miyoshi, T., Sawai, H., & Sato, H. (2013). Spatiotemporal receptive field

structures in retinogeniculate connections of cat. *Front. Syst. Neurosci.* 7, 103. doi: 10.3389/fnsys.2013.00103

Presentation

International

Sato, H., Naito, T., Osaka, H., Suematsu, N., Sadakane, O., Okamoto, M., & Shimegi, S. "Properties and mechanisms of orientation tuning of the cat lateral geniculate nucleus" 8th IBRO World Congress of Neuroscience, Firenze, Italy, 2011/7

Suematsu, N., Naito, T., & Sato, H. "Spatial-frequency and stimulus size dependent response modulation sharpens orientation tuning generated by elliptical receptive field in the cat lateral geniculate nucleus" Society for Neuroscience 2011, Washington, D.C., USA, 2011/11

Sato, H., Suematsu, N., Naito, T., Miyoshi, T., & Sawai, H. "Connection Principles Underlying the Spatio-Temporal Receptive Field Structure of Cat Retino-Geniculate Pathway" IUPS 2013, Birmingham, UK, 2013/7

Soma, S., Shimegi, S., Suematsu, N., Mizuyama, R., & Sato, H. "Functional role of acetylcholine in the primary visual cortex of rat" Society for Neuroscience 2013, San Diego, USA, 2013/11

Shimegi, S., Soma, S., Suematsu, N., Kimura, A., Sato, A., Yoshioka, D., & Sato, H. "The neural representation of brightness and its temporal dynamics in the cat primary visual cortex" Society for Neuroscience 2013, San Diego, USA, 2013/11

Naito, T., Suematsu, N., Miyoshi, T., Sawai, H., & Sato, H. “The statistical computation underlying surface property perception in the cat primary visual cortex” Society for Neuroscience 2013, San Diego, USA, 2013/11

Suematsu, N., Naito, T., Miyoshi, T., Sawai, H., & Sato, H. “Spatiotemporal receptive field structures in the retinogeniculate connections of the cat” Society for Neuroscience 2013, San Diego, USA, 2013/11

Domestic

末松尚史、内藤智之、佐藤宏道 “ネコ外側膝状体ニューロンの方位選択性と受容野時空間構造の関係 Relationship between orientation selectivity and spatiotemporal receptive field structure of the cat lateral geniculate neurons” 第33回日本神経科学大会（Neuro 2010）, 神戸, 2010/9

内藤智之、末松尚史、佐藤宏道 “ネコ外側膝状体における方位選択性と空間周波数選択性の時間変化 Temporal dynamics of orientation and spatial frequency tuning of neurons in the cat lateral geniculate nucleus” 第33回日本神経科学大会（Neuro 2010）, 神戸, 2010/9

末松尚史、内藤智之、佐藤宏道 “ネコ外側膝状体ニューロンの受容野時空間構造と方位選択性” 第103回近畿生理学談話会, 大阪, 2010/10

末松尚史、内藤智之、佐藤宏道 “ネコ外側膝状体ニューロンの受容野及び方位選択性の詳細検討” 視覚科学フォーラム第15回研究会, 大阪, 2011/8

末松尚史、内藤智之、佐藤宏道 “Relationship between orientation sensitivity and spatiotemporal receptive field structure of neurons in the cat lateral geniculate nucleus” 2011年度　包括脳ネットワーク夏のワークショップ, 神戸, 2011/8

末松尚史、内藤智之、佐藤宏道 “ネコ外側膝状体における方位選択性を形成する楕円形線形受容野と非線形応答修飾 Elliptical linear receptive field and non-linear response modulation generating orientation selectivity in the lateral geniculate nucleus of the cat” 第34回日本神経科学大会（Neuro 2011）, 神奈川, 2011/9

内藤智之、末松尚史、佐藤宏道 “刺激サイズおよび輝度コントラストの変化がヒトの視知覚における空間周波数チューニングに与える影響 The effect of stimulus size and luminance contrast on the spatial frequency tuning of the human visual perception” 第34回日本神経科学大会（Neuro 2011）, 神奈川, 2011/9

Suematsu, N., Naito, T., Miyoshi, T., Sawai, H., & Sato, H. “Retinogeniculate Connection and Elliptical Receptive Fields of Neurons in the Cat Lateral Geniculate Nucleus” 2012年度　包括脳ネットワーク夏のワークショップ, 宮城, 2012/7

相馬祥吾、七五三木聡、末松尚史、佐藤宏道 “ラット一次視覚野におけるコリン作動性視覚応答調節 Modulation of visual responses by acetylcholine in the rat primary visual cortex” 第35回日本神経科学大会（Neuro 2012）, 愛知, 2012/9

末松尚史、内藤智之、三好智満、澤井元、佐藤宏道 “ネコ外側膝状体ニューロンの楕円形受容野を形成する網膜 - 外側膝状体の機能的結合Retinogeniculate Connection Underlying the Elliptical

Receptive Fields of Neurons in the Cat Lateral Geniculate Nucleus” 第35回日本神経科学大会（Neuro 2012）, 愛知, 2012/9

末松尚史、内藤智之、三好智満、澤井元、佐藤宏道 “ネコ外側膝状体ニューロンの楕円形受容野と網膜-外側膝状体間結合の関係” 第105回近畿生理学談話会, 大阪, 2012/9

Soma, S., Suematsu N., & Shimegi, S. “Improvement of visual contrast detectability by a cholinesterase inhibitor in freely behaving rats” 2013年度　包括脳ネットワーク夏のワークショップ, 愛知, 2013/8

Yoshioka, D., Sato, A., Soma, S., Suematsu, N., Shimegi, S., & Sato, H. “Response-level-based surround suppression of the cat primary visual cortex” 2013年度　包括脳ネットワーク夏のワークショップ, 愛知, 2013/8

Awards

The Japan Society for the Promotion of Science Research Fellowships. 2013–2015.

Others

第22回生理科学実験技術トレーニングコース「ヒト脳機能マッピングにおけるデータ解析入門」, 自然科学研究機構生理学研究所, 2011/7

第23回生理科学実験技術トレーニングコース「生理学実験のための電気回路・機械工作・プログラミング(2)（C言語によるPICプログラミング）」, 自然科学研究機構生理学研究所, 2012/7

第24回生理科学実験技術トレーニングコース「生理学実験のための電気回路・機械工作・プログラミング(1)（生体アンプとバスチェンバーの作製）」, 自然科学研究機構生理学研究所, 2013/7